J Solid State Electrochem (2006) 10: 293–319
DOI 10.1007/s10008-006-0095-1

ORIGINAL PAPER

John Christensen · John Newman

Stress generation and fracture in lithium insertion materials

Received: 12 May 2005 / Revised: 9 December 2005 / Accepted: 20 December 2005 / Published online: 7 March 2006
© Springer-Verlag 2006

Abstract A mathematical model that calculates volume expansion and contraction and concentration and stress profiles during lithium insertion into and extraction from a spherical particle of electrode material has been developed. The maximum stress in the particle has been determined as a function of dimensionless current, which includes the charge rate, particle size, and diffusion coefficient. The effects of pressure-driven diffusion and nonideal interactions between the lithium and host material have also been described. The model predicts that carbonaceous particles will fracture in high-power applications such as hybrid-electric vehicle batteries.

Introduction

Particle fracture and electronic isolation of active electrode material is a potential failure mechanism in lithium-ion batteries. Volume changes in electrode particles during lithium insertion and extraction create stresses which may induce cracking. This is particularly evident in lithium alloys, which undergo volume changes of up to 300% of the nonlithiated electrode material [1]. Thomas [2] has suggested that the cracking of alloys and subsequent growth of a passivating film (the solid–electrolyte interphase) on the newly formed surface leads to isolation of active material from the conducting matrix.

Fracture has been observed in intercalation compounds as well. Ohzuku et al. [3] and Sawai et al. [4] observed the fracture of electrolytic manganese dioxide particles with an acoustic emission measurement technique. Their results indicate a higher rate of fracture at higher intercalation rates, especially during the first discharge, and little or no cracking during deintercalation. The former observation can be explained qualitatively by the high degree of lattice strain experienced by an insertion material with a large concentration gradient, which corresponds to high insertion rates.

Kostecki and McLarnon have observed that graphite particles near the separator in composite negative electrodes become more disordered with cycling [5]. A potential mechanism that is currently under investigation is that particles near the separator undergo higher rates of insertion and extraction, and thus higher stresses, than do those near the current collector. The high stresses in turn result in the structural degradation of graphite near the separator.

J. Christensen (✉) · J. Newman
Department of Chemical Engineering,
University of California,
Berkeley, CA 94720, USA
e-mail: jake.christensen@rtc.bosch.com
Tel.: +1-510-6431972
Fax: +1-510-6424778

Mathematical model

In the present work, we introduce a continuum model that describes the volume expansion and contraction of a spherical insertion material, as well as the stress distributions that arise from lithium intercalation. As illustrated in Fig. 1a, the outer shell of the particle expands as lithium is inserted, resulting in a strain differential between the inner and outer regions of the sphere. This strain differential, which increases with the rate of intercalation, gives rise to stress within the particle. If the stress surpasses the yield stress of the material, the particle will fracture.

As a first approximation, we assume that the electrode particle is disordered and that lithium diffusion and lattice expansion/contraction are isotropic. Approximating the particle as a sphere facilitates the use of a one-dimensional model.

Transport

First, we must understand how the electrode particle grows as it is charged with lithium. We treat the electrode material as a binary system in which LiS represents host material occupied with lithium and S represents unoccupied host material (e.g., C_6 for graphite).

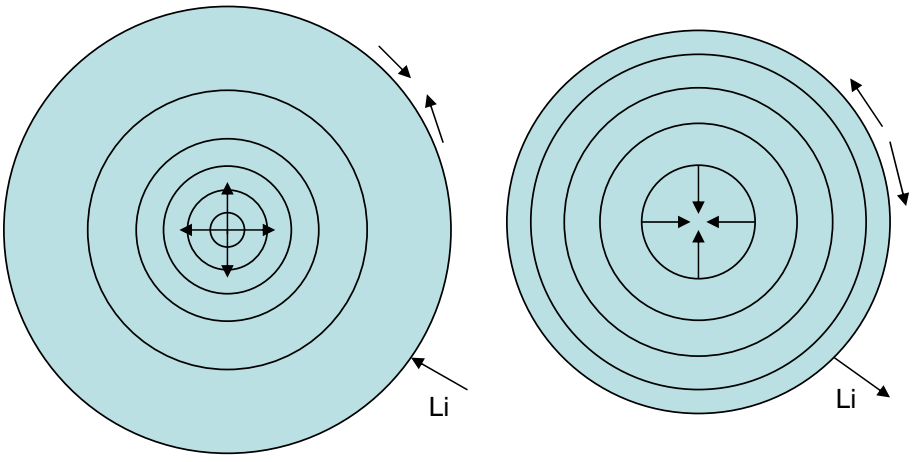

a Expansion (charge) b Contraction (discharge)

Fig. 1 Schematic of particle expansion during lithium insertion (e.g., during charge) and contraction during lithium extraction (e.g., during discharge). *Arrows pointing toward each other* indicate regions of compression in the particle, while *arrows pointing away from each other* indicate regions of tension. *Concentric circles* mark host-lattice tags, which are initially evenly spaced.

The thermodynamic driving force for species LiS, neglecting thermal diffusion, is [6, 7]

$$\underline{d}_{\mathrm{LiS}} = RT\frac{c_{\mathrm{LiS}}c_{\mathrm{S}}}{c\mathcal{D}_{\mathrm{LiS,S}}}(\underline{v}_{\mathrm{S}} - \underline{v}_{\mathrm{LiS}}) = c_{\mathrm{LiS}}\left(\nabla\mu_{\mathrm{LiS}} + \overline{S}_{\mathrm{LiS}}\nabla T - \frac{M_{\mathrm{LiS}}}{\rho}\nabla p\right), \tag{1}$$

where $\underline{v}_i$ and c_i are, respectively, the velocity and concentration of species i, μ_{LiS} is the chemical potential of species LiS, $\overline{S}_{\mathrm{LiS}}$ is the partial molar entropy of LiS, M_{LiS} is the molar mass of LiS, ρ is the density of the solution, $\mathcal{D}_{\mathrm{LiS,S}}$ is the binary diffusion coefficient due to a thermodynamic driving force, R is the gas constant, and p and T are the pressure and temperature, respectively. Recognizing that

$$d\mu_{\mathrm{LiS}} = \left(\frac{\partial\mu_{\mathrm{LiS}}}{\partial x_{\mathrm{LiS}}}\right)_{T,p,x_{\mathrm{S}}} dx_{\mathrm{LiS}} - \overline{S}_{\mathrm{LiS}}dT + \overline{V}_{\mathrm{LiS}}dp, \tag{2}$$

where x_{LiS} is the mole fraction of LiS [or state of charge (SOC)], and, using the definition of molar flux,

$$\underline{N}_i = c_i\underline{v}_{\mathrm{t}}, \tag{3}$$

we can rewrite Eq. (1) as

$$\underline{N}_{\mathrm{LiS}} = x_{\mathrm{LiS}}(\underline{N}_{\mathrm{LiS}} + \underline{N}_{\mathrm{S}}) - \frac{c_{\mathrm{LiS}}\mathcal{D}_{\mathrm{LiS,S}}}{RT} \times\left[\left(\frac{\partial\mu_{\mathrm{LiS}}}{\partial x_{\mathrm{LiS}}}\right)_{T,p,x_{\mathrm{s}}}\nabla x_{\mathrm{LiS}} + \left(\overline{V}_{\mathrm{LiS}} - \frac{M_{\mathrm{LiS}}}{\rho}\right)\nabla p\right], \tag{4}$$

where we have also used the fact that the mole fractions sum to one:

$$x_{\mathrm{LiS}} + x_{\mathrm{S}} = 1. \tag{5}$$

The chemical potential of LiS can be written as

$$\mu_{\mathrm{LiS}} = \mu^0_{\mathrm{LiS}} + RT\ln(\gamma_{\mathrm{LiS}}x_{\mathrm{LiS}}), \tag{6}$$

where μ^0_{LiS} is the chemical potential of LiS at a secondary reference state and γ_{LiS} is the activity coefficient of LiS. Thus,

$$\left(\frac{\partial\mu_{\mathrm{LiS}}}{\partial x_{\mathrm{LiS}}}\right)_{T,p,x_{\mathrm{S}}} = \frac{RT}{x_{\mathrm{LiS}}}\left(1 + \frac{\partial\ln\gamma_{\mathrm{LiS}}}{\partial\ln x_{\mathrm{LiS}}}\right). \tag{7}$$

Equation (4) becomes

$$\underline{N}_{\mathrm{LiS}} = x_{\mathrm{LiS}}(\underline{N}_{\mathrm{LiS}} + \underline{N}_{\mathrm{S}}) - c\mathcal{D}_{\mathrm{LiS,S}} \times\left[\left(1 + \frac{\partial\ln\gamma_{\mathrm{LiS}}}{\partial\ln x_{\mathrm{LiS}}}\right)\nabla x_{\mathrm{LiS}} + \frac{x_{\mathrm{LiS}}}{RT}\left(\overline{V}_{\mathrm{LiS}} - \frac{M_{\mathrm{LiS}}}{\rho}\right)\nabla p\right]. \tag{8}$$

We assume that the electrode particle is spherically symmetric so that, in radial coordinates, the flux law becomes

$$N_{\mathrm{LiS}} = x_{\mathrm{LiS}}(N_{\mathrm{LiS}} + N_{\mathrm{S}}) - c\mathcal{D}_{\mathrm{LiS,S}} \times\left[\left(1 + \frac{\partial\ln\gamma_{\mathrm{LiS}}}{\partial\ln x_{\mathrm{LiS}}}\right)\frac{\partial x_{\mathrm{LiS}}}{\partial r} + \frac{x_{\mathrm{LiS}}}{RT}\left(\overline{V}_{\mathrm{LiS}} - \frac{M_{\mathrm{LiS}}}{\rho}\right)\frac{\partial p}{\partial r}\right]. \tag{9}$$

In terms of the open-circuit potential (OCP), the thermodynamic factor is [see Eq. (133)]

$$\alpha_{\mathrm{LiS}} \equiv 1 + \frac{d\ln\gamma_{\mathrm{LiS}}}{d\ln x_{\mathrm{LiS}}} = -\frac{F}{RT}x_{\mathrm{LiS}}(1 - x_{\mathrm{LiS}})\frac{dU}{dx_{\mathrm{LiS}}}. \tag{10}$$

If U is a known function of x_{LiS}, then Eq. (10) is simply an algebraic equation that is coupled with Eq. (9).

The density can be expressed in terms of molar masses and mole fractions, such that Eq. (9) becomes

$$N_{\mathrm{LiS}} = x_{\mathrm{LiS}}(N_{\mathrm{LiS}} + N_{\mathrm{S}}) - c\mathcal{D}_{\mathrm{LiS,S}} \times \left[\alpha_{\mathrm{LiS}} \frac{\partial x_{\mathrm{LiS}}}{\partial r} + \frac{x_{\mathrm{LiS}}}{RT} \times \left(\overline{V}_{\mathrm{LiS}} - \frac{M_{\mathrm{LiS}}}{c[x_{\mathrm{LiS}} M_{\mathrm{LiS}} + (1 - x_{\mathrm{LiS}})M_{\mathrm{S}}]}\right) \frac{\partial p}{\partial r}\right]. \tag{11}$$

We assume that $\mathcal{D}_{\mathrm{LiS,S}}$ is approximately independent of mole fraction.

The continuity equations for species LiS and S are

$$\frac{\partial c x_{\mathrm{LiS}}}{\partial t} + \frac{1}{r^2}\frac{\partial}{\partial r}\left(r^2 N_{\mathrm{LiS}}\right) = 0 \tag{12}$$

and

$$\frac{\partial c(1 - x_{\mathrm{LiS}})}{\partial t} + \frac{1}{r^2}\frac{\partial}{\partial r}\left(r^2 N_{\mathrm{S}}\right) = 0. \tag{13}$$

The total concentration c should be, in general, a function of composition, pressure (or stress), and temperature. Because we assume the particle is isothermal, only variations in composition and stress must be considered. The concentration is separated into two parts: one composition dependent and one stress dependent. That is,

$$c = c_0(x_{\mathrm{LiS}})g[\mathrm{tr}(\mathbf{T})], \tag{14}$$

where tr (**T**) is the trace of the total stress tensor and c_0 is a function only of composition. The function g is defined in a subsequent section.

We calculate c_0 from the composition at a particular reference state (i.e., $T = 25°\mathrm{C}$ and $p = 1$ atm). One can think of c_0 as the reciprocal of the molar volume, which is expressed in terms of partial molar volumes as

$$\widetilde{V} = c_0^{-1} = x_{\mathrm{LiS}}\overline{V}_{\mathrm{LiS}} + x_{\mathrm{S}}\overline{V}_{\mathrm{S}}. \tag{15}$$

The assumption inherent in Eq. (14) is that the compressibility of the material is independent of composition. To our knowledge, the partial molar volumes have not been directly reported in the literature, but it may be possible to estimate them from lattice-parameter data. Many intercalation materials exhibit a linear relationship between lithium content and molar volume, implying constant partial molar volumes of both species. We shall therefore assume that both molar volumes are constant over the range $0 < x_{\mathrm{LiS}} < x_{\max}$, where $x_{\max}$ is the maximum SOC. The partial molar volume of S is set equal to the molar volume of pure host material at the reference state, which is determined from measurable physical properties:

$$\overline{V}_{\mathrm{S}} = \widetilde{V}^{\,0}_{\mathrm{S}} = \frac{M_{\mathrm{S}}}{\rho^0_{\mathrm{S}}}. \tag{16}$$

M_{S} and ρ^0_{S} are the molar mass and density, respectively, of vacant host material at the reference state. To estimate the partial molar volume of LiS, we recognize that, at $x_{\mathrm{LiS}} = x_{\max}$, the volume of the particle has expanded by a factor of $1+\omega$, where ω is the "fractional expansivity" of the particle. Hence, from Eq. (15), we have

$$(1 + \omega)\widetilde{V}_0 = x_{\max}\overline{V}_{\mathrm{LiS}} + (1 - x_{\max})\widetilde{V}^0_{\mathrm{S}}, \tag{17}$$

where $\widetilde{V}_0$ is the molar volume of the particle when it is devoid of lithium [i.e., the molar volume of pure S, given in Eq. (16)]. Rearranging, we have

$$\frac{\overline{V}_{\mathrm{LiS}}}{\widetilde{V}^0_{\mathrm{S}}} = \frac{\rho^0_{\mathrm{S}}}{M_{\mathrm{S}}}\overline{V}_{\mathrm{LiS}} = 1 + \frac{\omega}{x_{\max}}. \tag{18}$$

Equation (15) becomes

$$c_0^{-1} = \frac{M_{\mathrm{S}}}{\rho^0_{\mathrm{S}}}\left(1 + \frac{\omega}{x_{\max}} x_{\mathrm{LiS}}\right). \tag{19}$$

We can likewise modify Eq. (11):

$$N_{\mathrm{LiS}} = x_{\mathrm{LiS}}(N_{\mathrm{LiS}} + N_{\mathrm{S}}) - c\mathcal{D}_{\mathrm{LiS,S}} \times \left[\alpha_{\mathrm{LiS}} \frac{\partial x_{\mathrm{LiS}}}{\partial r} + \frac{x_{\mathrm{LiS}}}{RT}\left(\frac{M_{\mathrm{S}}}{\rho^0_{\mathrm{S}}}\left[1 + \frac{\omega}{x_{\max}}\right] - \frac{M_{\mathrm{LiS}}}{c[x_{\mathrm{LiS}} M_{\mathrm{LiS}} + (1 - x_{\mathrm{LiS}})M_{\mathrm{S}}]}\right)\frac{\partial p}{\partial r}\right]. \tag{20}$$

Coordinate transformation

Because the volume of the electrode particle changes during charge and discharge, we must transform our equations from the (r,t) coordinate system to the (ξ,t) coordinate system, where ξ is the dimensionless radial position:

$$\xi = \frac{r}{\mathcal{R}(t)}. \tag{21}$$

Here, $\mathcal{R}(t)$ is the radius of the particle, which varies with time.

We can transform any time derivatives as follows:

$$\left(\frac{\partial c}{\partial t}\right)_r = \left(\frac{\partial c}{\partial t}\right)_\xi + \left(\frac{\partial \xi}{\partial t}\right)_r \left(\frac{\partial c}{\partial \xi}\right)_t = \left(\frac{\partial c}{\partial t}\right)_\xi - \frac{\xi}{\mathcal{R}(t)}\frac{d\mathcal{R}}{dt}\left(\frac{\partial c}{\partial \xi}\right)_t. \tag{22}$$

Spatial derivatives are likewise transformed:

$$\left(\frac{\partial N}{\partial r}\right)_t = \left(\frac{\partial \xi}{\partial r}\right)_t \left(\frac{\partial N}{\partial \xi}\right)_t = \frac{1}{\mathcal{R}(t)}\left(\frac{\partial N}{\partial \xi}\right)_t. \tag{23}$$

Equations (12), (13), and (20) become

$$N_{\mathrm{LiS}} = x_{\mathrm{LiS}}(N_{\mathrm{LiS}} + N_{\mathrm{S}}) - \frac{c\mathcal{D}_{\mathrm{LiS,S}}}{\mathcal{R}}\left[\alpha_{\mathrm{LiS}}\frac{\partial x_{\mathrm{LiS}}}{\partial \xi} + \frac{x_{\mathrm{LiS}}}{RT}\left(\frac{M_{\mathrm{S}}}{\rho_{\mathrm{S}}^0}\left[1 + \frac{\omega}{x_{\max}}\right] - \frac{M_{\mathrm{LiS}}}{c[x_{\mathrm{LiS}}M_{\mathrm{LiS}} + (1 - x_{\mathrm{LiS}})M_{\mathrm{S}}]}\right)\frac{\partial p}{\partial \xi}\right], \tag{24}$$

$$\frac{\partial c x_{\mathrm{LiS}}}{\partial t} - \xi\frac{\partial \mathcal{R}}{\partial t}\frac{\partial c x_{\mathrm{LiS}}}{\partial \xi} + \frac{1}{\mathcal{R}\xi^2}\frac{\partial}{\partial \xi}\left(\xi^2 N_{\mathrm{LiS}}\right) = 0, \tag{25}$$

and

$$\frac{\partial c(1 - x_{\mathrm{LiS}})}{\partial t} - \xi\frac{\partial \mathcal{R}}{\partial t}\frac{\partial c(1 - x_{\mathrm{LiS}})}{\partial \xi} + \frac{1}{\mathcal{R}\xi^2}\frac{\partial}{\partial \xi}\left(\xi^2 N_{\mathrm{S}}\right) = 0, \tag{26}$$

where we have dropped the subscripts on all partial derivatives, it being implied that ξ and t are now the independent variables of interest.

Displacement and the lattice velocity

We define the displacement, u, to be the difference between the radial position, $r'(r_0, t)$, of a lattice element at time t, and the initial radial position, r_0, of that lattice element. That is,

$$u = r' - r_0. \tag{27}$$

We can think of r_0 as a lattice tag for crystallographic unit cells of host material, which consists of a mixture of S and LiS. The tagged cells can always be referenced to their initial position, r_0, despite the fact that their position at a later time may change. The circles drawn in Fig. 1 denote the positions of lattice tags after the particle has been deformed during lithium insertion or extraction.

The correct definition of the lattice velocity is the rate of change in displacement for a tagged cell with initial position r_0. In other words, it is the rate of change of displacement at constant r_0. Note that, according to Eq. (27), this is also equal to the rate of change in the radial position of a lattice element at constant initial position. Hence,

$$v_{\mathrm{L}} = \left(\frac{\partial u}{\partial t}\right)_{r_0} = \left(\frac{\partial r'}{\partial t}\right)_{r_0}. \tag{28}$$

The lattice velocity can also be defined in terms of lithium-occupied host sites (LiS), lithium-unoccupied host sites (S), and host-lattice vacancies (V_{s}). A lithium-unoccupied host site and a host-lattice vacancy are here defined to mean two different types of sites. The former is a unit of host material (e.g., C_6) that does not contain lithium, while the latter is a void where the unit of host material should be. According to Battaglia [8], the flux of host-lattice vacancies relative to their convective flux is equal and opposite to the total flux of filled lattice sites (both S and LiS) relative to their convective flux:

$$N_{\mathrm{LiS}} + N_{\mathrm{S}} - cv_{\mathrm{L}} = -(N_{V_{\mathrm{s}}} - c_{V_{\mathrm{s}}}v_{\mathrm{L}}), \tag{29}$$

where V_{s} is the Kröger–Vink notation [9, 10] for a host-lattice vacancy (e.g., a void where a C_6 unit should be). We assume that, for host-lattice sites, there are no such vacancies, so that the flux and concentration of vacancies are zero. Thus,

$$\frac{N_{\mathrm{LiS}} + N_{\mathrm{S}}}{c} = v_{\mathrm{L}}. \tag{30}$$

To evaluate the time derivative of u given in Eq. (28), we make use of the definition of displacement [Eq. (27)] and the partial-derivative identity:

$$\left(\frac{\partial X}{\partial Y}\right)_Z\left(\frac{\partial Y}{\partial Z}\right)_X\left(\frac{\partial Z}{\partial X}\right)_Y = -1. \tag{31}$$

Hence,

$$\left(\frac{\partial r'}{\partial t}\right)_{r_0} = -\frac{\left(\frac{\partial r_0}{\partial t}\right)_{r'}}{\left(\frac{\partial r_0}{\partial r'}\right)_t} = \frac{\left(\frac{\partial u}{\partial t}\right)_{r'}}{1 - \left(\frac{\partial u}{\partial r'}\right)_t}. \tag{32}$$

Combining Eqs. (28), (30), and (32) yields

$$\frac{N_{\mathrm{LiS}}+N_{\mathrm{S}}}{c}=\frac{\left(\frac{\partial u}{\partial t}\right)_{r'}}{1-\left(\frac{\partial u}{\partial r'}\right)_{t}}. \tag{33}$$

Because there is a one-to-one correspondence between the radial position, r', of an element and that element's position along the radial coordinate, r, we can drop the primes in Eq. (33), leaving

$$\frac{N_{\mathrm{LiS}}+N_{\mathrm{S}}}{c}=\frac{\left(\frac{\partial u}{\partial t}\right)_{r}}{1-\left(\frac{\partial u}{\partial r}\right)_{t}}. \tag{34}$$

We now have the lattice velocity in the r–t coordinate system, which must be transformed to the ξ–t coordinate system. For convenience, we use the definition

$$w=\left(\frac{\partial u}{\partial r}\right)_{t}=\frac{1}{\mathcal{R}}\left(\frac{\partial u}{\partial \xi}\right)_{t}. \tag{35}$$

In terms of the independent variables ξ and t, the lattice velocity equation becomes

$$\frac{N_{\mathrm{LiS}}+N_{\mathrm{S}}}{c}=\frac{\left(\frac{\partial u}{\partial t}\right)_{\xi}-w\xi\frac{d\mathcal{R}}{dt}}{1-w}. \tag{36}$$

Finally, we note that the total radius of the particle is dependent only on time, and not on position within the particle:

$$\frac{d\mathcal{R}}{d\xi}=0. \tag{37}$$

At this point we have nine dependent variables: $\mathcal{R}$, u, w, x_{LiS}, N_{LiS}, N_{S}, c, p, and α_{LiS}; and eight governing equations: Eqs. (10), (19), (24), (25), (26), (35), (36), and (37). To supplement these equations, we require some insight into the internal forces on the host material due to lattice expansion and contraction.

Solid mechanics

To describe fully the physical picture portrayed here, we must relate the radial displacement of material to the stress and pressure in the particle, as well as incorporate the stress into our equation of state for the concentration. Thus, we must formulate equations for strain and stress distributions in the sphere.

For finite displacement, the Eulerian strain is given by [11]

$$\mathbf{E}^{*}=\frac{1}{2}\left[\mathbf{I}-\left(\mathbf{X}\overleftarrow{\nabla}_{\mathbf{x}}\right)^{T}\cdot\mathbf{X}\overleftarrow{\nabla}_{\mathbf{x}}\right], \tag{38}$$

where $\mathbf{I}$ is the identity tensor. $\mathbf{X}$ is the initial position of a volume element in its undeformed state and $\mathbf{x}$ is the current position of the element in the deformed material. All momentum and mass balances are written in an Eulerian formulation, that is, in terms of the position $\mathbf{x}$.

The relationship between the initial and current positions of a volume element is

$$\mathbf{X}=\mathbf{x}-\mathbf{u}, \tag{39}$$

where $\mathbf{u}$ is the displacement vector. We can therefore write Eq. (38) as

$$\mathbf{E}^{*}=\frac{1}{2}\left(\mathbf{I}-\overrightarrow{\nabla}_{\mathbf{x}}\mathbf{x}\cdot\mathbf{x}\overleftarrow{\nabla}_{\mathbf{x}}+\overrightarrow{\nabla}_{\mathbf{x}}\mathbf{x}\cdot\mathbf{u}\overleftarrow{\nabla}_{\mathbf{x}}+\overrightarrow{\nabla}_{\mathbf{x}}\mathbf{u}\cdot\mathbf{x}\overleftarrow{\nabla}_{\mathbf{x}}-\overrightarrow{\nabla}_{\mathbf{x}}\mathbf{u}\cdot\mathbf{u}\overleftarrow{\nabla}_{\mathbf{x}}\right). \tag{40}$$

Note that, regardless of the coordinate system,

$$\frac{\partial x_i}{\partial x_j}=\delta_{ij}, \tag{41}$$

where δ_{ij} is the Kronecker delta. Thus, we have

$$\mathbf{x}\overleftarrow{\nabla}_{\mathbf{x}}=\overrightarrow{\nabla}_{\mathbf{x}}\mathbf{x}=\begin{bmatrix}1&0&0\\0&1&0\\0&0&1\end{bmatrix}=\mathbf{I}, \tag{42}$$

and the Eulerian strain can be written

$$\mathbf{E}^{*}=\frac{1}{2}\left(\mathbf{u}\overleftarrow{\nabla}_{\mathbf{x}}+\overrightarrow{\nabla}_{\mathbf{x}}\mathbf{u}-\overrightarrow{\nabla}_{\mathbf{x}}\mathbf{u}\cdot\mathbf{u}\overleftarrow{\nabla}_{\mathbf{x}}\right). \tag{43}$$

In spherical coordinates, for an arbitrary vector $\mathbf{a}$,

$$\mathbf{a}\overleftarrow{\nabla}=\begin{bmatrix}\frac{\partial a_r}{\partial r} & \frac{1}{r}\frac{\partial a_r}{\partial \theta}-\frac{a_\theta}{r} & \frac{1}{r\sin\theta}\frac{\partial a_r}{\partial \phi}-\frac{a_\phi}{r}\\ \frac{\partial a_\theta}{\partial r} & \frac{1}{r}\frac{\partial a_\theta}{\partial \theta}+\frac{a_r}{r} & \frac{1}{r\sin\theta}\frac{\partial a_\theta}{\partial \phi}-\frac{a_\phi}{r}\cot\theta\\ \frac{\partial a_\phi}{\partial r} & \frac{1}{r}\frac{\partial a_\phi}{\partial \theta} & \frac{1}{r\sin\theta}\frac{\partial a_\phi}{\partial \phi}+\frac{a_\theta}{r}\cot\theta+\frac{a_r}{r}\end{bmatrix}. \tag{44}$$

and

$$\overrightarrow{\nabla}\mathbf{a}=\left(\mathbf{a}\overleftarrow{\nabla}\right)^{T}. \tag{45}$$

We can write out the required gradient tensors in Eq. (43) in a simplified fashion by noting that our spherical particle is

symmetric with respect to θ and ϕ, and that the only nonzero component of displacement is u_r. Hence, the gradient of the displacement vector becomes

$$\mathbf{u}\overleftarrow{\nabla}_{\mathbf{x}} = \overrightarrow{\nabla}_{\mathbf{x}}\mathbf{u} = \begin{bmatrix} \dfrac{\partial u_r}{\partial r} & 0 & 0 \\ 0 & \dfrac{u_r}{r} & 0 \\ 0 & 0 & \dfrac{u_r}{r} \end{bmatrix}. \tag{46}$$

Substituting these tensors into Eq. (43), we have

$$\mathbf{E}^* = \begin{bmatrix} \dfrac{\partial u_r}{\partial r} - \dfrac{1}{2}\left(\dfrac{\partial u_r}{\partial r}\right)^2 & 0 & 0 \\ 0 & \dfrac{u_r}{r} - \dfrac{1}{2}\left(\dfrac{u_r}{r}\right)^2 & 0 \\ 0 & 0 & \dfrac{u_r}{r} - \dfrac{1}{2}\left(\dfrac{u_r}{r}\right)^2 \end{bmatrix}. \tag{47}$$

The radial strain is thus

$$\varepsilon_{\mathrm{r}} \equiv E_{rr} = \frac{\partial u}{\partial r} - \frac{1}{2}\left(\frac{\partial u}{\partial r}\right)^2, \tag{48}$$

and the tangential strain is

$$\varepsilon_{\mathrm{t}} \equiv E_{\theta\theta} = E_{\phi\phi} = \frac{u}{r} - \frac{1}{2}\frac{u^2}{r^2}, \tag{49}$$

where we have dropped the subscript from the radial displacement. In spherical coordinates, the dilatational strain is given by the trace of the strain tensor

$$e = \mathrm{tr}(\mathbf{E}) = \varepsilon_{\mathrm{r}} + 2\varepsilon_{\mathrm{t}} = \frac{\partial u}{\partial r} + \frac{2u}{r} - \frac{1}{2}\left(\frac{\partial u}{\partial r}\right)^2 - \frac{u^2}{r^2}, \tag{50}$$

The normal radial stress is given by Hooke's law:

$$\begin{aligned} \sigma_{\mathrm{r}} &= \lambda e + 2\mu\varepsilon_{\mathrm{r}} \\ &= (\lambda + 2\mu)\left[\frac{\partial u}{\partial r} - \frac{1}{2}\left(\frac{\partial u}{\partial r}\right)^2\right] + 2\lambda\left(\frac{u}{r} - \frac{1}{2}\frac{u^2}{r^2}\right), \end{aligned} \tag{51}$$

where λ and μ are the Lamé constants [11]. The normal tangential stresses are given by

$$\begin{aligned} \sigma_{\mathrm{t}} &= \lambda e + 2\mu\varepsilon_{\mathrm{t}} \\ &= \lambda\left[\frac{\partial u}{\partial r} - \frac{1}{2}\left(\frac{\partial u}{\partial r}\right)^2\right] + 2(\lambda + \mu)\left(\frac{u}{r} - \frac{1}{2}\frac{u^2}{r^2}\right). \end{aligned} \tag{52}$$

The stresses defined here are the elastic components of stress, with the sign convention that compressive stresses are negative and tensile stresses are positive. This is the sign convention commonly used in the field of solid mechanics, but is the opposite of that encountered in much of the chemical engineering literature [12]. The total stress is the difference between the elastic stress and the thermodynamic pressure:

$$T_i = \sigma_i - p. \tag{53}$$

This total stress is what should be compared to the yield stress of a material to determine whether fracture is likely to occur.

Equations (51), (52), and (53) constitute a modified version of Hooke's law. The standard formulation relates the strain directly to the total stress, which is taken to be purely elastic. The modification is necessary due to the fact that strain is created both by elastic stress and by variation in composition. Some other authors [13, 14] divide the strain in exactly this manner, with the strain given as the sum of a stress component, given by Hooke's law, and a temperature- [13] or concentration-dependent [14] term, which can be considered thermodynamic. Our approach is equivalent, but instead divides the stress into two components, one elastic (σ_i) and the other thermodynamic (p). The equivalence is shown by Timoshenko, who calculates thermal stress in a solid using both formulations [13]. Our approach is somewhat more general, in that the thermodynamic pressure, p, is not restricted to be equivalent to the mean normal pressure, which is related to the trace of the total stress tensor.

In terms of the elastic (Young's) modulus (E), Poisson's ratio (ν), the variable w [see Eq. (35)], and the dimensionless radial coordinate (ξ), Eqs. (51) and (52) become

$$\begin{aligned} \sigma_{\mathrm{r}} = &\frac{E}{(1+\nu)(1-2\nu)} \\ &\times \left[(1-\nu)\left(w - \frac{1}{2}w^2\right) + 2\nu\left(\frac{u}{\xi\mathcal{R}} - \frac{1}{2}\frac{u^2}{\xi^2\mathcal{R}^2}\right)\right] \end{aligned} \tag{54}$$

and

$$\sigma_{\mathrm{t}} = \frac{E}{(1+\nu)(1-2\nu)}\left[\nu\left(w - \frac{1}{2}w^2\right) + \frac{u}{\xi\mathcal{R}} - \frac{1}{2}\frac{u^2}{\xi^2\mathcal{R}^2}\right]. \tag{55}$$

Because both of these equations contain singularities at ξ=0, we must calculate their limits as ξ approaches zero. This involves the use of l'Hôpital's rule along with Eq. (35). We find that

$$\sigma_{\mathrm{r}} = \sigma_{\mathrm{t}} = \frac{E}{(1-2\nu)}\left(w - \frac{1}{2}w^2\right) \tag{56}$$

at $\xi = 0$. Equation (56) is used in the numerical solution, but it is not strictly a boundary condition.

To complete our set of equations, we must define the pressure within the particle. Neglecting gravitational and other body forces, the momentum balance within the particle is

$$\frac{\partial(\sigma_r - p)}{\partial r} + \frac{2}{r}(\sigma_r - \sigma_t) = \rho \frac{\partial^2 u}{\partial t^2}. \tag{57}$$

This second-order partial differential equation must be transformed to the (ξ,t) coordinate system. It is convenient to introduce the variable

$$z = \left(\frac{\partial u}{\partial t}\right)_r = \left(\frac{\partial u}{\partial t}\right)_\xi - w\xi \frac{d\mathcal{R}}{dt}. \tag{58}$$

In terms of this new variable and previously defined dependent variables and parameters, Eq. (57) is transformed to yield

$$\frac{\partial(\sigma_r - p)}{\partial \xi} + \frac{2}{\xi}(\sigma_r - \sigma_t) = c\mathcal{R}[x_{LiS}M_{LiS} + (1 - x_{LiS})M_S] \times \left(\frac{\partial z}{\partial t} - \frac{\xi}{\mathcal{R}}\frac{d\mathcal{R}}{dt}\frac{\partial z}{\partial \xi}\right). \tag{59}$$

The right side of the equation constitutes the inertial terms. These are negligible in the present application, as discussed later. Note that without the use of the variable z, the second order time derivative would be written as

$$\left(\frac{\partial^2 u}{\partial t^2}\right)_r = \frac{\partial^2 u}{\partial t^2} - 2\xi\frac{d\mathcal{R}}{dt}\frac{\partial w}{\partial t} - w\xi\frac{d^2\mathcal{R}}{dt^2} + \frac{\xi}{\mathcal{R}}\left(\frac{d\mathcal{R}}{dt}\right)^2\left(2w + \xi\frac{\partial w}{\partial \xi}\right). \tag{60}$$

Not only is this a more cumbersome substitution, but the second order time derivatives would require a computationally expensive central-difference time-stepping technique.

Finally, we must determine the dependence of concentration upon stress. To derive the function g in Eq. (14), we begin with the definition of the isothermal compressibility of a fluid:

$$\kappa = -\frac{1}{\delta V}\frac{\partial(\delta V)}{\partial p}, \tag{61}$$

where δV is the volume of an element of the fluid and p is the pressure. For the solid material we consider here, we replace the pressure with minus one-third the trace of the total stress tensor:

$$\overline{p} = -\frac{\mathrm{tr}(\mathbf{T})}{3}. \tag{62}$$

The pressure defined here is the mean normal pressure, which is generally not identical to the thermodynamic pressure, p, used in Eq. (61) [11]. However, using this definition of the pressure allows us to define a compressibility in terms of the elastic modulus and Poisson's ratio that is consistent with Hooke's law. Equation (61) becomes

$$\frac{\kappa}{3} = \frac{1}{\delta V}\frac{\partial(\delta V)}{\partial \mathrm{tr}(\mathbf{T})}. \tag{63}$$

For a material with finite strain, the deformed volume is related to the undeformed volume and the elements of strain by [11, 15]

$$\delta V = \delta V_0\sqrt{1 + 2(\varepsilon_1 + \varepsilon_2 + \varepsilon_3) + 4(\varepsilon_1\varepsilon_2 + \varepsilon_1\varepsilon_3 + \varepsilon_2\varepsilon_3) + 8\varepsilon_1\varepsilon_2\varepsilon_3}. \tag{64}$$

In spherical coordinates, $\varepsilon_1 = \varepsilon_r$ and $\varepsilon_2 = \varepsilon_3 = \varepsilon_t$.

For the dependence of concentration upon stress, we neglect variations in composition, those being contained in c_0. Hence, the components of strain can be related directly to the components of total stress by Hooke's law:

$$\varepsilon_r = \frac{1}{E}(T_r - 2\nu T_t), \tag{65}$$

$$\varepsilon_t = \frac{1}{E}[(1 - \nu)T_t - \nu T_r]. \tag{66}$$

We make use of the fact that the two components of stress should be of the same order of magnitude as the trace of the stress tensor. Hence, Eq. (64) becomes

$$\delta V = \delta V_0\left[1 + \frac{(1 - 2\nu)\mathrm{tr}(\mathbf{T})}{E}\right] + \mathrm{O}\left(\frac{[\mathrm{tr}(\mathbf{T})]^2}{E^2}\right). \tag{67}$$

As long as the components of the total stress are much smaller than the elastic modulus, we can neglect terms of order $\mathrm{tr}(\mathbf{T})^2/E^2$ and higher. Equations (63) and (67) yield

$$\frac{\kappa}{3} = \frac{(1 - 2\nu)}{E + 2(1 - 2\nu)\mathrm{tr}(\mathbf{T})}. \tag{68}$$

We would like to use a best constant value for the compressibility; therefore, we use

$$\kappa = \frac{3(1-2\nu)}{E}, \tag{69}$$

which should be valid for stresses much smaller than the elastic modulus. Note that E and ν, and therefore κ, are, in general, dependent upon composition. However, in the absence of specific measured data, we take them to be constant. This allows us to partition the concentration according to Eq. (14).

In terms of the total concentration of the element, Eq. (63) becomes

$$\frac{\kappa}{3} = -\frac{1}{c}\frac{\partial c}{\partial \mathrm{tr}(\mathbf{T})}. \tag{70}$$

Hence, for a constant value of κ, the concentration is given by

$$\begin{aligned} c &= c_0 \exp\left(-\frac{\kappa \mathrm{tr}(\mathbf{T})}{3}\right) \\ &= c_0 \exp\left[-\frac{(1-2\nu)(\sigma_r + 2\sigma_t - 3p)}{E}\right]. \end{aligned} \tag{71}$$

We can now combine the stress and composition dependences of the concentration [Eqs. (19) and (71)] into a single equation of state:

$$c^{-1} = \frac{M_S}{p_s^0}\left(1 + \frac{\omega}{x_{max}} x_{LiS}\right) \exp\left[\frac{(1-2\nu)(\sigma_r + 2\sigma_t - 3p)}{E}\right]. \tag{72}$$

There are now 12 variables (R, u, w, z, x_{LiS}, N_{LiS}, N_S, c, σ_r, σ_t, p, and α_{LiS}) governed by 12 highly coupled and nonlinear equations [Eqs. (10), (24), (25), (26), (35), (36), (37), (54), (55), (58), (59), and (72)].

Boundary conditions

Equations (24), (25), (26), (35), (37), and (59) are first-order differential equations in position, each of which requires an appropriate boundary condition.

The gradient in lithium mole fraction is set by the current density at the edge of the sphere. Because the area of the particle changes, the current density for galvanostatic charge or discharge must be related to the total current delivered to the particle, I_p, which is constant under galvanostatic conditions. For our purposes, the electrode consists of a single particle, but nonuniform current distributions throughout the electrode, and hence, variation in I_p from one particle to the next, even under galvanostatic conditions, must be taken into account in porous electrodes. Furthermore, the current density is not, in general, uniform over the surface of a single particle, and the local stress should be higher where the current density is above the average. We assume that the current is distributed evenly over the surface of the particle, implying that our simulations yield a best-case scenario for particle fracture. For a real particle, particularly one that is not spherical, fracture should occur at a lower charge rate than is predicted here.

The current density at the particle surface is given by

$$i = \frac{I_p}{4\pi \mathcal{R}^2}. \tag{73}$$

$\mathcal{R}$ is the radius of the particle at a particular time. Thus, the boundary condition for Eq. (24) is

$$r^2\left(N_{LiS} - c x_{LiS}\frac{dr}{dt}\right) = -\frac{I_p}{4\pi F} \text{ at } \xi = 1, \tag{74}$$

where F is Faraday's constant. The left side of the equation is obtained by subtracting the convective flux of LiS from its total molar flux. We need not transform the time derivative in Eq. (74), because it is here defined at a fixed value of ξ (i.e., that corresponding to the particle surface). Note that r and $\mathcal{R}$ are identical at this point.

For Eqs. (25) and (26), we set the flux of each component to zero at the center of the sphere:

$$N_{LiS} = 0 \text{ at } \xi = 0, \tag{75}$$

$$N_S = 0 \text{ at } \xi = 0. \tag{76}$$

For Eq. (35), one might be tempted to use the condition that the radial displacement at the center of the sphere is zero:

$$u = 0 \text{ at } \xi = 0. \tag{77}$$

However, this is not independent of Eq. (36) in the limit as ξ goes to zero. Thus, we must use a suitable boundary condition for w at the center. Differentiating Eq. (55) with respect to ξ and taking the limit as ξ goes to zero, we find

$$\frac{\partial \sigma_t}{\partial \xi} = \frac{E\nu}{(1+\nu)(1-2\nu)}(1-w)\frac{\partial w}{\partial \xi} \text{ at } \xi = 0. \tag{78}$$

Thus, if we assume that the derivatives of the stress components are zero at the center (i.e., there is no discontinuity in the slope of the stress as we pass through the center), then we can use the boundary condition

$$\frac{\partial w}{\partial \xi} = 0 \text{ at } \xi = 0. \tag{79}$$

To determine the radius of the particle in Eq. (37), we note that the rate of change in the total radius of the particle is simply the rate of change in displacement at the surface of the particle:

$$\frac{d\mathcal{R}}{dt} = \frac{\partial u}{\partial t} \text{ at } \xi = 1. \tag{80}$$

Finally, for the momentum balance [Eq. (59)], we apply a radial force balance at the particle surface:

$$\sigma_r - p + p_0 = 0 \text{ at } \xi = 1, \tag{81}$$

where p_0 is the external hydrostatic pressure.

Equation (77) can be used in place of Eq. (36) at $\xi = 0$, although it is not considered a boundary condition. Moreover, Eq. (36) takes the form

$$\frac{N_{LiS} + N_S}{c} = \frac{\partial u}{\partial t} \tag{82}$$

in the limit, as ξ approaches one. This equation is obtained by substituting Eq. (80) into Eq. (36). We refer to Eqs. (56), (77), and (82) as alternate boundary equations. They do not meet the strict definition of a boundary condition, but are special limits of the associated governing equations. Like boundary conditions, they are implemented at boundary mesh points.

Nondimensionalization

It is quite illuminating and convenient to nondimensionalize the equations that govern particle expansion and contraction. Equation (21) defines the dimensionless spatial coordinate, while

$$\tau = \frac{t\mathcal{D}_{LiS,S}}{\mathcal{R}_0^2} \tag{83}$$

is the appropriate dimensionless temporal coordinate, where $\mathcal{R}_0$ is the initial radius of the particle. The dimensionless dependent variables are

$$\mathcal{N}_i = \frac{N_i \mathcal{R}_0 M_S}{\mathcal{D}_{LiS,S}\rho_S^0}, \tag{84}$$

$$\theta = \frac{cM_S}{\rho_S^0}, \tag{85}$$

$$\chi = \frac{\mathcal{R}}{\mathcal{R}_0}, \tag{86}$$

$$\overline{u} = \frac{u}{\mathcal{R}_0}, \tag{87}$$

$$\overline{\sigma}_i = \frac{\sigma_i(1+\nu)(1-2\nu)}{E}, \tag{88}$$

$$\pi = \frac{(p-p_0)(1+\nu)(1-2\nu)}{E}, \tag{89}$$

and

$$\zeta = \frac{z\mathcal{R}_0}{\mathcal{D}_{LiS,S}}. \tag{90}$$

Although it is not considered one of our dependent variables, we nondimensionalize the OCP as well:

$$\overline{U} = \frac{FU}{RT}. \tag{91}$$

The variables x_{LiS}, w, and α_{LiS} are already dimensionless.

Equations (10), (24), (25), (26), (35), (36), (37), (54), (55), (56), (58), (59), (72), (74), (75), (76), (80), (81) and (82) become

$$\alpha_{LiS} = -x_{LiS}(1 - x_{LiS})\frac{d\overline{U}}{dx_{LiS}}, \tag{92}$$

$$\mathcal{N}_{LiS} = x_{LiS}(\mathcal{N}_{LiS} + \mathcal{N}_S) - \frac{\theta}{\chi}\left[\alpha_{LiS}\frac{\partial x_{LiS}}{\partial \xi} + ex_{LiS}\left(1 + \frac{\omega}{x_{max}} - \frac{\overline{M}}{\theta\left[x_{LiS}\overline{M} + (1 - x_{LiS})\right]}\right)\frac{\partial \pi}{\partial \xi}\right], \tag{93}$$

$$\frac{\partial \theta x_{\mathrm{LiS}}}{\partial \tau} - \xi \frac{\partial \chi}{\partial \tau} \frac{\partial \theta x_{\mathrm{LiS}}}{\partial \xi} + \frac{1}{\chi \xi^2} \frac{\partial}{\partial \xi} \left(\xi^2 \mathcal{N}_{\mathrm{LiS}} \right) = 0, \tag{94}$$

$$\frac{\partial \theta (1 - x_{\mathrm{LiS}})}{\partial \tau} - \xi \frac{\partial \chi}{\partial \tau} \frac{\partial \theta (1 - x_{\mathrm{LiS}})}{\partial \xi} + \frac{1}{\chi \xi^2} \frac{\partial}{\partial \xi} \left(\xi^2 \mathcal{N}_{\mathrm{s}} \right) = 0, \tag{95}$$

$$w = \frac{1}{\chi} \frac{\partial \overline{u}}{\partial \xi}, \tag{96}$$

$$\frac{\mathcal{N}_{\mathrm{LiS}} + \mathcal{N}_{\mathrm{s}}}{\theta} = \frac{\frac{\partial \overline{u}}{\partial \tau} - w \xi \frac{d\chi}{d\tau}}{1 - w}, \tag{97}$$

$$\frac{d\chi}{d\xi} = 0, \tag{98}$$

$$\overline{\sigma}_{\mathrm{r}} = (1 - \nu) \left(w - \frac{1}{2} w^2 \right) + 2\nu \left(\frac{\overline{u}}{\xi \chi} - \frac{1}{2} \frac{\overline{u}^2}{\xi^2 \chi^2} \right), \tag{99}$$

$$\overline{\sigma}_{\mathrm{t}} = \nu \left(w - \frac{1}{2} w^2 \right) + \frac{\overline{u}}{\xi \chi} - \frac{1}{2} \frac{\overline{u}^2}{\xi^2 \chi^2}, \tag{100}$$

$$\overline{\sigma}_{\mathrm{r}} = \overline{\sigma}_{\mathrm{t}} = \left(w - \frac{1}{2} w^2 \right) \text{ at } \xi = 0, \tag{101}$$

$$\zeta = \frac{\partial \overline{u}}{\partial \tau} - w \xi \frac{d\chi}{d\tau}, \tag{102}$$

$$\frac{\partial (\overline{\sigma}_{\mathrm{r}} - \pi)}{\partial \xi} + \frac{2}{\xi} (\overline{\sigma}_{\mathrm{r}} - \overline{\sigma}_{\mathrm{t}}) = D \theta \chi \left[x_{\mathrm{LiS}} \overline{M} + (1 - x_{\mathrm{LiS}}) \right] \left(\frac{\partial \zeta}{\partial \tau} - \frac{\xi}{\chi} \frac{d\chi}{d\tau} \frac{\partial \zeta}{\partial \xi} \right), \tag{103}$$

$$\theta^{-1} = \left(1 + \frac{\omega}{x_{\max}} x_{\mathrm{LiS}} \right) \exp \left(\frac{\overline{\sigma}_{\mathrm{r}} + 2\overline{\sigma}_{\mathrm{t}} - 3\pi}{1 + \nu} \right), \tag{104}$$

$$\chi^2 \left(\mathcal{N}_{\mathrm{LiS}} - \theta x_{\mathrm{LiS}} \frac{d\chi}{d\tau} \right) = -I \text{ at } \xi = 1, \tag{105}$$

$$\mathcal{N}_{\mathrm{LiS}} = 0 \text{ at } \xi = 0, \tag{106}$$

$$\mathcal{N}_{\mathrm{s}} = 0 \text{ at } \xi = 0, \tag{107}$$

$$\frac{d\chi}{d\tau} = \frac{\partial \overline{u}}{\partial \tau} \text{ at } \xi = 1, \tag{108}$$

$$\overline{\sigma}_{\mathrm{r}} - \pi = 0 \text{ at } \xi = 1, \tag{109}$$

and

$$\frac{\mathcal{N}_{\mathrm{LiS}} + \mathcal{N}_{\mathrm{s}}}{\theta} = \frac{\partial \overline{u}}{\partial \tau.} \tag{110}$$

Six principal dimensionless parameters fall out of the analysis, including Poisson's ratio (ν), the dimensionless current,

$$I = \frac{I_{\mathrm{p}} M_{\mathrm{s}}}{4\pi \mathcal{R}_0 F \mathcal{D}_{\mathrm{LiS,s}} \rho_{\mathrm{s}}^0}, \tag{111}$$

the partial molar volume ratio,

$$\overline{V}_{\mathrm{LiS}}^{*} \equiv \frac{\overline{V}_{\mathrm{LiS}}}{\overline{V}_{\mathrm{s}}} = \frac{\rho_{\mathrm{s}}^0 \overline{\mathrm{V}}_{\mathrm{LiS}}}{M_{\mathrm{s}}} = 1 + \frac{\omega}{x_{\max}}, \tag{112}$$

the ratio,

$$D = \frac{\mathcal{D}_{\mathrm{LiS,s}}^2 \rho_{\mathrm{s}}^0 (1 + \nu)(1 - 2\nu)}{\mathcal{R}_0^2 E}, \tag{113}$$

the dimensionless Young's modulus,

$$e = \frac{E M_{\mathrm{s}}}{\rho_{\mathrm{s}}^0 R T (1 + \nu)(1 - 2\nu)}, \tag{114}$$

and the molar-mass ratio,

$$\overline{M} = \frac{M_{\mathrm{LiS}}}{M_{\mathrm{s}}}. \tag{115}$$

Note that these last two parameters vanish when we neglect pressure-driven diffusion. There is also an as yet unspecified number of dimensionless parameters contained in the OCP–SOC relationship that determines the value of the activity coefficient. D can be thought of as the ratio of diffusive to elastic energy, and e as the ratio of elastic to thermal energy. For a typical carbonaceous particle, D is on the order of 10^{-22}, and the inertial term in Eq. (103) can be neglected.

Equations (77), (79), (92), (93), (94), (95), (96), (97), (98), (99), (100), (101), (103), (104), (105), (106), (107), (108), (109), and (110) were posed in finite-difference form and solved with the BAND(j) subroutine. Equation (102) was excluded because D is negligible, and therefore the equations for ζ become uncoupled from the remaining 11 equations. A BAND map of the equations is given in Fig. 2. Altogether, there are 11 variables and 11 governing equations, including 6 that are first order in ξ (or y), for which six boundary conditions are employed: 3 at the center of the sphere, and 3 at the surface. A Crank–Nicolson timestepping approach was employed, giving an error that is of order $(\Delta\xi)^2$ in the spatial direction and $(\Delta\tau)^2$ in the temporal direction. Forty-one spatial mesh points were used and were shown to give sufficient accuracy. Increasing the number of mesh points lengthened the computation time and generated significant round-off errors. At higher dimensionless currents, simulations with a large number of mesh points (≥100) exhibited instability.

The simulation interval up to the end of lithium insertion/extraction was divided into roughly 1,100 timesteps (for the galvanostatic mode). The first 250 timesteps were limited to approximately 5×10^{-6}, depending upon the dimensionless current, so that peaks in the maximum stress (see Fig. 6) could be resolved. Subsequently, the time increment was doubled after every 20 timesteps until a maximum increment of 0.15 was reached. Under some conditions, particularly those in which the assumption of ideality is relaxed, the number of timesteps was increased to improve the resolution of certain regions of interest. For simulations of long dimensionless duration, corresponding to small dimensionless current, the maximum increment was increased to 0.5. Note that timesteps are dimensionless.

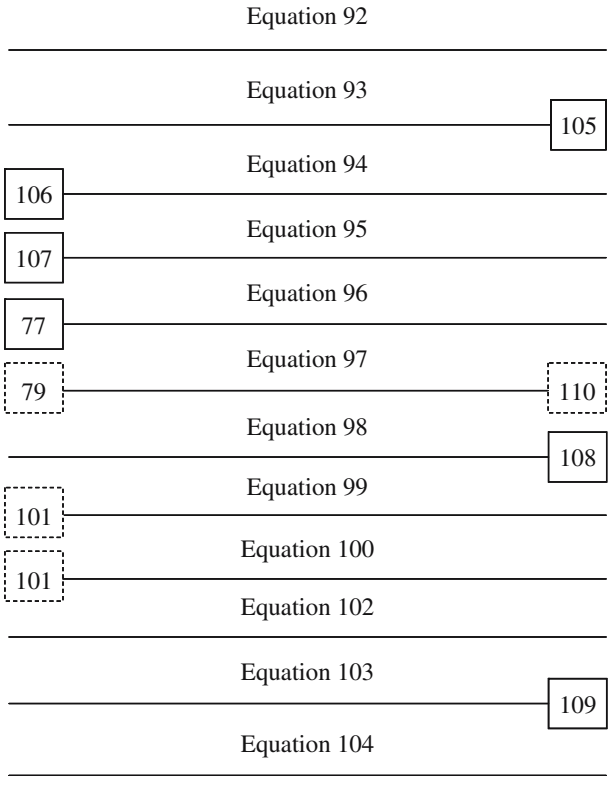

Fig. 2 Map of equations that are solved numerically. *Solid-boxed equations* are boundary conditions and *dash-boxed equations* are limiting forms of governing equations.

Results and discussion

Ideal solutions

Now that we have a general framework for volume change and stress evolution in isotropic spherical particles due to lithium insertion and extraction, we make two more simplifying approximations. We assume that the thermodynamic factor is equal to 1 (i.e., the OCP is purely Nernstian), and we neglect the inertial term in the momentum balance because the dimensionless parameter, D, is small. The former simplification, which is relaxed in later sections, eliminates the need for Eq. (92), while the latter eliminates the need for Eq. (102). This reduces our set of equations and variables to 10 each; thus, speeding the simulations. Unless otherwise noted, the results that follow reflect these approximations.

Figures 3, 4, 5, 6, and 7 apply to simulations of a carbonaceous particle that expands during lithium insertion. The properties and other parameters used for the simulations are given in Table 1. The particle size, diffusivity, and density are representative of a wide class of carbonaceous materials, including mesophase carbon microbeads (MCMB), which are frequently used in lithium-ion batteries. These materials are generally more disordered and, therefore, more isotropic than natural graphite, and their capacity is generally lower than that of natural graphite, although this depends upon the heat-treatment temperature [16]. The elastic modulus is

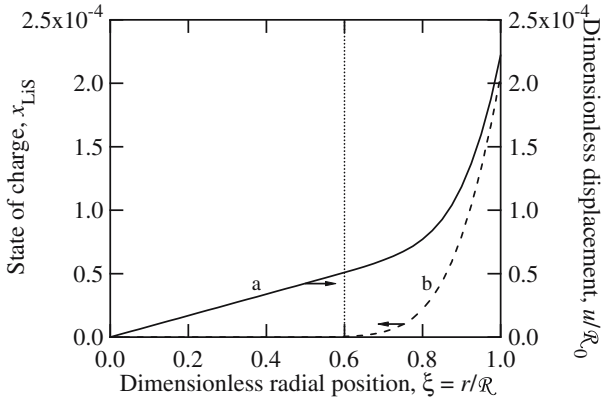

Fig. 3 Radial profiles of **a** the dimensionless current and **b** the SOC after 0.9 s of lithium insertion at a C/3 charge rate. The *vertical dotted line* divides regions of pure elastic deformation and concentration deformation. The parameters used in the simulation are listed in Table 1.

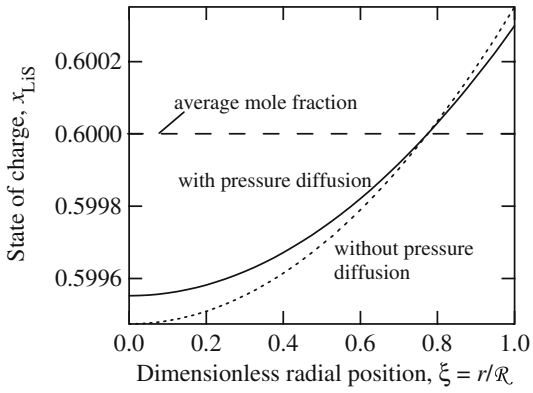

Fig. 4 Simulated concentration profiles for lithium in the particle, as a function of the dimensionless radial position, at the end of lithium insertion. The *solid curve* includes the influence of pressure-driven diffusion, while the *dotted curve* neglects this driving force. The *dashed line* indicates the average mole fraction of lithium-occupied sites in the particle, corresponding to a SOC of 0.6. The parameters used in the simulation are listed in Table 1.

representative of isotropic graphites, [17] while the Poisson ratio is typical of most solid materials. The simlations were terminated once the average SOC in the particle reached 0.6 (i.e., $Li_{0.6}C_6$). Measured and calculated lattice parameters for graphite indicate that the lattice volume increases by 13 to 14% (10 to 11% for the inner-layer spacing and 1 to 2% in the transverse directions) during full lithium insertion ($C_6 \rightarrow LiC_6$), and that the variation is approximately linear with respect to lithium composition [18–20]. Hence, it was assumed that the particle volume increased by 8% over the course of the simulation ($\omega = 0.08$).

Despite the anisotropy of expansion for a single graphitic grain, it is assumed that particles are disordered and consist of enough grains that the overall volume

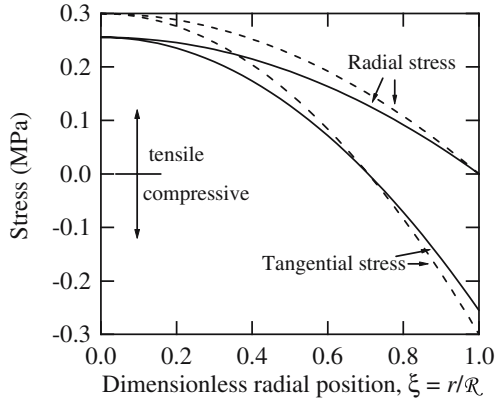

Fig. 5 Simulated normal stress profiles in the particle, as a function of dimensionless radial position, at the end of lithium insertion. Positive values indicate tensile stresses, while negative values correspond to compression. The *solid curves* include the effect of pressure-driven diffusion, while the *dashed curves* neglect it. The parameters used in the simulation are listed in Table 1.

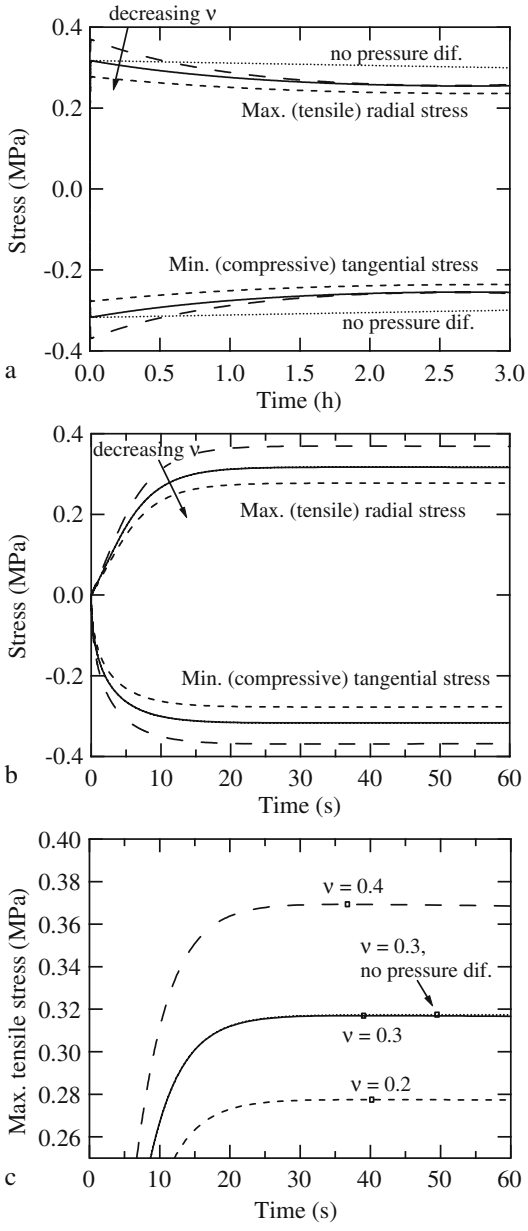

Fig. 6 Maximum normal radial stresses (at ξ=0) and minimum normal tangential stresses (at ξ=1) during lithium insertion. The *dotted curves* correspond to a simulation with ν=0.3, in which pressure diffusion is neglected, while the *dashed and solid curves* correspond to simulations that include pressure diffusion, with ν=0.2, 0.3, and 0.4, as indicated. All other parameters are given in Table 1. Plots **b** and **c** show the stresses at short times, and the *open squares* in plot **c** mark the maximum tensile stress obtained for each simulation.

expansion is isotropic. Anisotropic carbons, such as natural graphite, may be more suited to a prismatic (rather than spherical) model, in which the material primarily expands in the direction perpendicular to lithium diffusion. In this case, the stress in the particle should be somewhat less, because the material is not constrained by a spherical geometry. The stress generated in an actual particle should fall somewhere between the spherical and prismatic extremes.

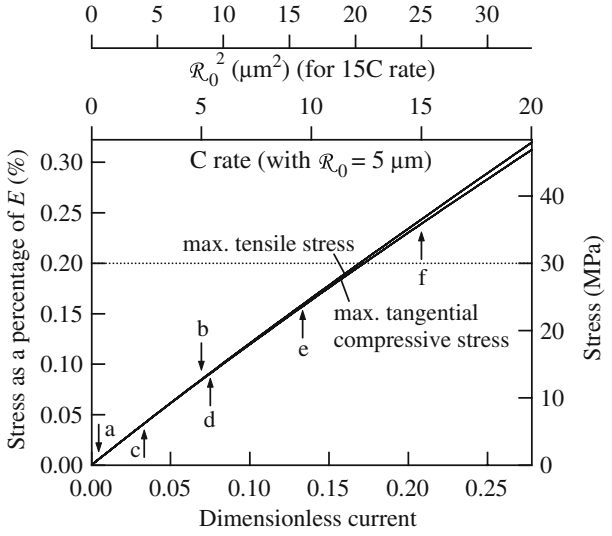

Fig. 7 Magnitude of the maximum tensile and compressive stresses encountered during lithium insertion, both as a percentage of E (*left axis*) and in absolute terms (*right axis*), as a function of dimensionless current. The upper axes give the corresponding C rate for a 5-μm particle radius and the square of the radius for a 15C rate. For $\mathcal{R}_0$=5 μm, *arrows a* and *b* correspond to C/3 and 5C rates, respectively. For a 15C rate, *arrows c* through *f* correspond to particle radii of 2, 3, 4, and 5 μm. The *dotted line* marks the approximate yield strength of the material.

Rather than list the current that is delivered to the particle in Table 1, we record the C rate, or inverse of the time required for full insertion. This is a better standard for comparison of particles with different radii than the current per particle. In terms of previously defined quantities, the C rate is

$$C = \frac{I_p M_S}{\frac{4}{3}\pi \mathcal{R}_0^3 F \rho_s^0 \Delta x}, \tag{116}$$

where Δx is the change in SOC for complete charge or discharge of the particle. For the carbonaceous material considered here, the minimum SOC is zero, and $\Delta x = \pm x_{max}$. Hence, the dimensionless current defined in Eq. (111) becomes

$$I = \pm \frac{C \mathcal{R}_0^2 x_{max}}{3 \mathcal{D}_{LiS,S}}. \tag{117}$$

In terms of the dimensionless time required for full insertion, the dimensionless current is

$$I = \frac{x_{max}}{3 \tau_{max}}. \tag{118}$$

From Eq. (111), one might erroneously draw the conclusion that decreasing the particle size will result in an increase in the dimensionless current, when in fact, the opposite is true because I_p depends upon particle size.

Table 1 Parameters and corresponding dimensionless groups used in the simulations

Parameter	Value	Dimensionless parameter	Value
x_{LiS0}	0	I	1.667×10^{-3}
$\mathcal{R}_0$ (μm)	3	$\overline{V}^*_{LiS}$	1.1333
$\mathcal{D}_{LiS,S}$ (m^2/s)	10^{-13}	e	399.5
$\alpha_{LiS,S}$	1	$\overline{M}$	1.09632
ω	0.08	D	8.09×10^{-23}
C (h^{-1})	0.333 (or C/3)		
E (GPa)	15		
ν	0.3		
M_{LiS} (g/mol)	79.001		
M_S (g/mol)	72.06		
ρ_s^0 (g/cm^3)	2.1		
x_{max}	0.6		

Figure 3 shows the concentration profile and dimensionless displacement profile after 0.9 s of lithium insertion at the C/3 rate. At this time, the concentration profile has not yet been fully established, and there is essentially no lithium in the core of the particle ($\xi < 0.6$). However, there is a positive displacement in this region due to the tension created by the expanded shell. The vertical dotted line in the figure divides the particle into two regions; to the left of the line, the strain is almost entirely elastic, while to the right, the strain is a combination of elastic strain and strain due to a compositional expansion of the lattice. The displacement is a linear function of radial position in the purely elastic region, satisfying the standard Hooke's law and momentum balance equations for spheres with uniform radial surface tension.

Figure 4 shows the lithium mole fraction profile in the particle at the end of lithium insertion. For comparison, the profile that is obtained when pressure diffusion is neglected is also shown. The dashed line marks the average mole fraction in the particle. As might be expected, the variation in composition is significantly smaller when pressure diffusion is included because there is a substantial variation of the pressure in the particle. The pressure gradient acts to reduce the lithium concentration gradient, thereby lowering the mechanical stress and, in turn, minimizing the pressure gradient until a balance is obtained. Even when pressure diffusion is neglected, the mole fraction varies by less than a 10th of a percent throughout the particle. This is because the insertion rate used for this simulation is relatively low, corresponding to a charge rate of C/3 (3-h charge) for a 3-μm particle.

Figure 5 shows tangential and radial stress profiles for the same pair of simulations. The stress variation is almost 20% greater when pressure diffusion is neglected. This underscores the importance of including the pressure-diffusion term in our analysis.

The stresses plotted in Fig. 5 are total stresses, as given in Eq. (53). The radial stress is tensile in the center of the particle and goes to zero at the surface because it is defined

relative to the external pressure on the particle. The tangential stress is tensile and equal to the radial stress at the center of the sphere, but is compressive at the particle's surface. The equality of the two stress components at the center is the consequence of their coincident directionality at $r=0$.

The tensile vs compressive nature of the stress components can be explained as follows: the outer part of the spherical particle is swollen with lithium relative to the inner part of the sphere. Thus, the lattice constant for the host material is greater near the surface than it is near the center. This lattice mismatch has the effect of pulling at the (relatively) lithium-poor inner part, both radially and tangentially, and tangentially pushing together the lithium-rich outer part, as illustrated in Fig. 1a.

Figure 6a shows how the maximum (tensile) radial and minimum (compressive) tangential stresses in the particle vary as lithium is intercalated for a few different cases. The dotted curves correspond to the simulation in which pressure diffusion is neglected, and the solid and dashed curves correspond to simulations that include pressure diffusion with three different values of ν, 0.2, 0.3, and 0.4, as indicated in the figure.

Although the stresses at the end of lithium insertion are much greater when pressure diffusion is neglected, the maximum stress that is obtained near the beginning of lithium insertion is comparable in both cases, as is apparent in Fig. 6c. A clue to the more rapid decline in stress for the pressure-diffusion case can be found in the binary diffusion equation [Eq. (93)], in which the pressure gradient is multiplied by the mole fractions of lithium and host material. As the mole fraction of lithium increases during insertion, the pressure-diffusion term becomes more dominant, resulting in a more uniform lithium concentration and, therefore, smaller stress. The pressure-diffusion effect is diminished near the end of insertion due to the monotonic decrease in particle density [see Eq. (9)]. This is exhibited by a leveling off of the stress extrema and a slight increase in their magnitude after 2.5 h.

The pressure-diffusion effect should disappear entirely at SOCs near one. This can be verified easily by substituting Eq. (104) into Eq. (93) to show that the factor in front of the pressure gradient vanishes for $x_{\mathrm{LiS}}=0$ and

$$x_{\mathrm{LiS}}=\frac{\overline{M}\exp\left(\frac{\overline{\sigma}_{\mathrm{r}}+2\overline{\sigma}_{\mathrm{t}}-3\pi}{1+\nu}\right)-1-\frac{\omega}{x_{\max}}}{\left(\overline{M}-1\right)\left(1+\frac{\omega}{x_{\max}}\right)-\overline{M}\frac{\omega}{x_{\max}}\exp\left(\frac{\overline{\sigma}_{\mathrm{r}}+2\overline{\sigma}_{\mathrm{t}}-3\pi}{1+\nu}\right)}. \tag{119}$$

The exact value of the above root depends upon the dimensionless current, but in any case, the exponential is near unity, and therefore, so is the corresponding root. This relationship would be different if variable partial molar volumes were used. It can be shown that the pressure-diffusion term also vanishes in the limit $x_{\mathrm{LiS}}\to\infty$. The fact that there are three roots means that the pressure driving force can contribute to diffusion both positively and negatively. In this particular case, $\omega/x_{\max}>\overline{M}$, but if the opposite were true, the pressure-diffusion contribution would be reversed.

The figure shows that the maximum stress increases with ν. As ν increases, a material resists changes in volume more than it resists changes in shape. A value of $\nu=0.5$ corresponds to an incompressible solid. The spherical geometry of the particle considered here constrains the material such that the overall shape does not change, but the size varies according to the concentration of lithium. Hence, a material with a higher Poisson ratio should undergo greater stress. Using a mathematical lens, it is clear from Eqs. (54) and (55) that the factor $E/(1+\nu)/(1-2\nu)$ blows up as ν approaches 0.5, resulting in higher stresses for a given displacement. The higher stress results in a higher hydrostatic pressure, which is why the effect of pressure diffusion is more pronounced for simulations with higher values of ν. The magnitudes of the stress components for $\nu=0.4$ even dip below those obtained for $\nu=0.3$.

Figure 6b and c are expanded plots of the first minute of lithium insertion. It is apparent that the maximum (or minimum) in stress is not highly dependent upon whether pressure diffusion is included. It is interesting to note that the radial stress maxima, marked as boxes in Fig. 6c, are obtained between 35 and 50 s, corresponding roughly to the time at which the lithium concentration profile becomes fully developed. This makes intuitive sense; as the overall concentration difference through the particle increases, the stress also increases. After the initial increase, the stress curves level off on this time scale, indicative of the establishment of a pseudo-steady-state concentration profile. There are two relevant timescales at play. The timescale for diffusion, given by $\mathcal{R}_0^2/\mathcal{D}_{\mathrm{LiS,S}}$, governs the establishment of the concentration profile, while the timescale for full lithium insertion is $1/C$. Note that the ratio of these two timescales is contained in the dimensionless current. For the present simulations, $\mathcal{R}_0^2/\mathcal{D}_{\mathrm{LiS,S}}=90\,\mathrm{s}$ and $1/\mathrm{C}=3$ h. A consequence of these disparate timescales is that, after a few minutes, the stress evolution does not depend upon the precise initial conditions (e.g., whether the concentration profile is initially uniform). At higher dimensionless currents, these two timescales become more equivalent, and the initial conditions play a larger role.

Furthermore, pseudo-steady-state stresses can be obtained, or nearly obtained, during charges or discharges on the order of 10 s in duration which are typical in the driving profile of an electric vehicle or hybrid-electric vehicle (HEV). The peak stress that is obtained depends more on the SOC and the C rate than on the duration of charge/discharge.

Figure 6b also shows that the peak in tensile radial stress (at the center of the sphere) somewhat lags the peak in compressive tangential stress. The maximum value of $x_{\mathrm{LiS}}(\xi=1)-x_{\mathrm{LiS}}(\xi=0)$ occurs somewhere between the two peaks. This delay is illustrated further by the lower initial slope of the tensile stress compared to that of the compressive stress. It arises because changes in the flux of

lithium into or out of the particle propagate from the surface of the sphere to the center.

It is clear why the stress decreases in magnitude after full development of the concentration profile when pressure diffusion is included in the analysis. However, as is evident in Fig. 6a, there is also a slight drop in the magnitude of the stress components even when pressure diffusion is neglected. This drop is due to the fact that as the radius of the particle increases, the current density at the surface must fall off as $1/\mathcal{R}^2$ to maintain the same overall rate of lithium insertion (i.e., the same superficial current density). Thus, neglecting the convective flux, the flux of lithium in the particle at the surface of the particle is proportional to $1/\mathcal{R}^2$ [see Eq. (74)]. As the flux decreases, the concentration gradient through the particle likewise decreases, and thus, the stress in the particle drops.

Whether the solid particle will fracture during lithium insertion depends upon the maximum stress that is encountered in the material. It is clear that this maximum is reached shortly after insertion begins. Although their moduli vary widely, yield strengths of carbonaceous materials are typically 0.2 to 1% of the Young's modulus [17]. Thus, the 0.25 to 0.4 MPa peak stresses represented in Fig. 6 are well below the yield stress for a material with Young's modulus of 15 GPa, and we should not expect the particle to fracture under the simulated conditions.

It is insightful to track the maximum stress as a function of the lithium insertion rate. Figure 7 shows the maximum tensile stress (at the center of the sphere) and the maximum compressive tangential stress (at the surface of the sphere) encountered during insertion as a function of the dimensionless current given in Eq. (117). The right axis gives the absolute stress in MPa, for a 15 GPa modulus material, and the left axis gives the stress as a fraction of the modulus. The dimensionless current is given on the lower axis, while the two upper axes give the corresponding charge rate (for a 5-μm particle) and particle size (for a 15C insertion rate). It is clear from the figure that the maximum stress increases with dimensionless current, as expected. According to Eq. (117), this means that the stress increases with both the rate of insertion and the particle size, but decreases when the diffusivity of lithium increases. Of the dimensionless parameters, the C rate, particle size, and diffusivity appear only in I and κ, the latter of which is negligible, so their influence is captured in its entirety by Fig. 7.

It is worth noting that the tensile stress is greater than the compressive stress for all values of I. Most materials have a much higher compressive yield stress than tensile yield stress; therefore, our results indicate that, during lithium insertion, the particle is much more likely to fracture under tension (starting near the center) than under compression (starting at the surface).

Turning our focus to the C rates shown in Fig. 7, we see that a 5C rate (arrow b) results in a stress that is an order of magnitude greater than that which is produced at a C/3 rate (arrow a). The former corresponds to a charge rate of 12 min, which is typical of the rate requirements for an HEV, while the latter, a 3-h charge, is more typical of an electric vehicle application. Although the stress is much higher for the 5C rate, it is still below the yield stress of the material (indicated, approximately, by the dotted line in Fig. 7). However, the yield stresses of materials are generally lowered by repeated strain cycling [21], and it is possible that the yield stress of carbonaceous materials will fall below 30 MPa when the lithium-ion cell is cycled. Moreover, nonuniform current densities in a porous electrode imply that some particles will be charged at rates higher than the average. Increasing the charge rate further to 15C (arrow f) brings the maximum stress into the region in which fracture is likely, even in the absence of cycling.

Winter et al. [22] suggest that cracking in alloy particles can be avoided by selecting a small enough particle size. We postulate that this critical size decreases as the charge/discharge rate requirements for a given application are increased. One could conceive of a porous electrode reaching this state naturally as it is cycled, with the particles cracking until they are below the critical size.

Arrows c, d, e, and f correspond to particle radii of 2, 3, 4, and 5 μm, respectively, for a 15C rate of lithium insertion. We see that a moderate reduction in the particle size has a dramatic effect on the mechanical stress, lowering it well below the yield stress of the material. Smaller particles would therefore appear to be more suitable for high-power applications, although a tradeoff must be considered. When smaller particles are used, the electrochemical surface area is greater, and so is the amount of lithium that is consumed during formation of the solid electrolyte interphase [23, 24]. The degree of solvent cointercalation may also be greater for smaller particles, particularly if the proportion of edge sites close to basal planes is high [24].

To avoid belaboring the obvious, we have not shown explicitly the dependence of the maximum tensile and compressive stresses upon the diffusion coefficient, which is contained in the dimensionless current. However, it is worth remarking on the fact that the stress decreases as the diffusion coefficient is raised, because a fairly prevalent method for accelerated life studies of lithium-ion cells is to raise the temperature. The argument for doing so is that the higher temperature will hasten the degradation mechanisms responsible for cell failure (e.g., capacity loss due to side reactions), and predictions can be made about the life of the cells at the normal operating temperature without waiting many years for them to fail. However, if particle fracture caused by volume expansion and contraction is a major contributor to cell failure, raising the temperature, and thereby the diffusion coefficient of lithium, should actually prolong the life of the cell by lowering the stresses generated in the particles. A more general statement is that, by raising the temperature, one runs the risk of underemphasizing failure modes that are dominant at the desired operating temperature.

Lithium extraction

To make a comparison between the lithium insertion and extraction results, we use the same nominal radius and nominal current densities in both cases. The nominal radius is the radius of the particle in the lithium-depleted state, and the nominal current density is the current density at the beginning of insertion or the end of extraction.

Figure 8 shows the components of stress in the particle at the end of lithium extraction, defined as the point at which the lithium concentration falls to zero at the surface of the particle, with the same nominal current density and particle size used to generate Figs. 3 and 4. The components of stress at the end of lithium insertion are shown for comparison. Both simulations include the effect of pressure diffusion. The two sets of stresses contain similar features, but compression occurs toward the center of the sphere and tangential tension occurs near the surface during extraction, as illustrated in Fig. 1b. Because crack formation is more likely due to tension than compression, the most likely point of fracture during extraction is at the surface.

Figure 9 shows the change in maximum (tensile) tangential and minimum (compressive) radial stresses during lithium extraction, both with and without pressure diffusion. For comparison, the stresses that arise during lithium insertion for the same set of parameters are reproduced from Fig. 6. The dimensionless times required for full insertion vs extraction are approximately related by the two-thirds power of the degree of expansion, $(1+\omega)^{2/3}$. The dimensionless time required for extraction is slightly less than $(1+\omega)^{-2/3}$ times that required for insertion because extraction is stopped once the concentration of lithium at the surface falls to zero. The average concentration in the particle is always greater than zero.

It is clear from Fig. 9a that the maximum stress is reached at the very end of lithium extraction. The reason for a continuous increase in the stress during extraction is tantamount to the reason for a continuous decrease (after full concentration development) during insertion. As the particle shrinks, the current density (and, therefore, flux of lithium) increases, and the greater concentration gradient leads to a higher stress. These trends are related to the manner in which lithium is inserted/extracted (i.e., galvanostatically), and do not necessarily hold for other charge/discharge modes.

The magnitudes of the stress components with pressure diffusion included (curves ii and iii) start out lower than the corresponding stress magnitudes when pressure diffusion is neglected (curves i and iv), but the extrema at the end of lithium extraction are almost identical because the pressure term vanishes as x_{LiS} approaches zero.

Figure 9b compares the stresses during the first minute of extraction (solid curves) to those during the first minute of insertion (dashed curves), with the insertion curves without pressure diffusion omitted for clarity. The symmetry is striking; as with the insertion stresses, the increase in magnitude of the radial stress at the center of the sphere (curves iii and iv) lags the increase in magnitude of the tangential stress at the surface of the sphere.

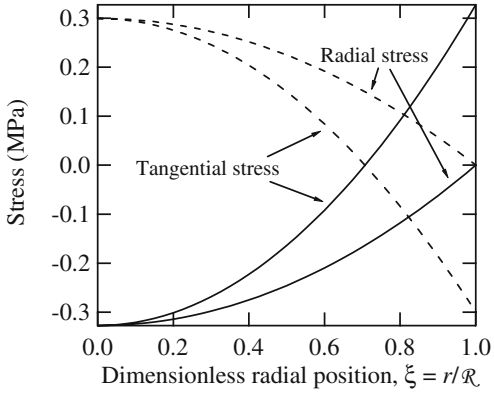

Fig. 8 Simulated stress profiles in the particle at the end of lithium insertion (*dashed curves*) and at the end of lithium extraction (*solid curves*). Both sets of curves include the effect of pressure-driven diffusion. The parameters used are given in Table 1, except that the initial SOC is 0.6 and the sign of the dimensionless current is reversed for the extraction simulation. In each case, the composition is initially uniform.

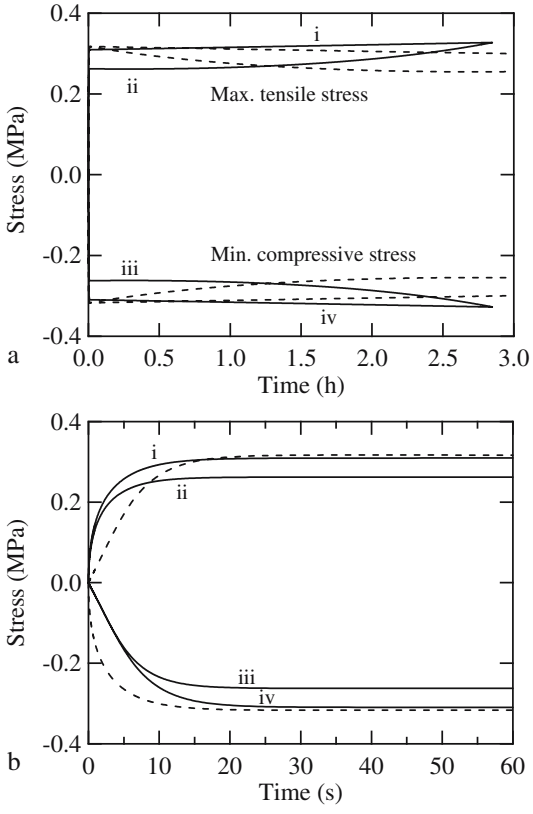

Fig. 9 Maximum normal tangential stresses (at ξ=1) and minimum normal radial stresses (at ξ=0) during lithium extraction (*solid curves*), with the corresponding curves for lithium insertion (*dashed curves*) reproduced from Fig. 5 for comparison. Plot **b** shows the same results on an expanded time scale. The curves are labeled as follows: *i* tangential stress at ξ=1, no pressure term; *ii* tangential stress at ξ=1, with pressure term; *iii* radial stress at ξ=0, with pressure term; *iv* radial stress at ξ=0, no pressure term. For clarity, the curves for lithium insertion with no pressure diffusion are omitted from plot **b**. The simulation parameters are given in Table 1.

External pressure

In the results presented so far, it has been assumed implicitly that the pressure external to the particle is zero, indicated by the fact that the total radial stress goes to zero at the particle surface. However, if we applied an external pressure, the stress curves would be shifted in the negative (compressive) direction, as shown in Fig. 10. Additional external pressure would reduce the maximum tensile stress that is obtained at a given dimensionless current while increasing the maximum compressive stress, as shown in Fig. 11. Because tensile strengths are generally lower than compressive strengths, such a strategy could delay or prevent the onset of particle fracture. A marginal increase in the allowable dimensionless current due to an incremental increase in external pressure can be calculated from the slope of the curve, $d\sigma_i/dI$, at any given stress level. In particular, at the 30 MPa level, marked by the dotted line, 5 MPa of external pressure increases the allowable dimensionless current by 0.030 (18%). We point out that 5 MPa is roughly 50 atm and, likely, is much greater than the pressures that are typically applied to cells; therefore, increasing the pressure so dramatically is not a practically viable strategy.

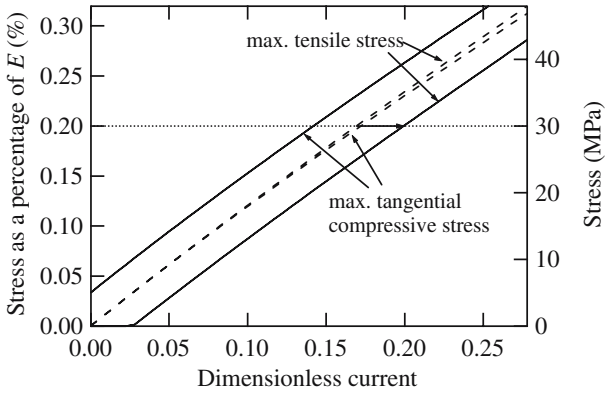

Fig. 11 Maximum tensile and compressive stresses encountered during lithium insertion, with no external pressure (*dashed curves*) and with an applied pressure of 5 MPa (*solid curves*). The *horizontal arrow* along the *dotted line* indicates that, upon application of 5 MPa of pressure, the dimensionless current can be increased by 18% while maintaining a maximum tensile stress that is 0.2% of the elastic modulus.

Nonideal solutions

We now turn our attention to nonidealities in the solid solution that manifest themselves in both the thermodynamic factor and the exchange current density, the latter of which is relevant under potentiostatic conditions. Both of these quantities are derived in the Appendix.

To model these nonidealities, we start with an empirical fit for the OCP of MCMB graphite,[1] given by

$$
\begin{aligned}
U(x_{\mathrm{LiS}}) = {} & 0.124 + 1.5\exp\left(-150x_{\mathrm{LiS}}\right) + 0.0155\tanh\left(\frac{x_{\mathrm{LiS}}-0.105}{0.029}\right) - 0.011\tanh\left(\frac{x_{\mathrm{LiS}}-0.124}{0.0226}\right) \\
& - 0.102\tanh\left(\frac{x_{\mathrm{LiS}}-0.194}{0.142}\right) + 0.0347\tanh\left(\frac{x_{\mathrm{LiS}}-0.286}{0.083}\right) - 0.0147\tanh\left(\frac{x_{\mathrm{LiS}}-0.5}{0.034}\right) \\
& - 0.0045\tanh\left(\frac{x_{\mathrm{LiS}}-0.9}{0.119}\right) - 0.022\tanh\left(\frac{x_{\mathrm{LiS}}-0.98}{0.0164}\right) - 0.035\tanh\left(\frac{x_{\mathrm{LiS}}-0.99}{0.05}\right).
\end{aligned}
\tag{120}
$$

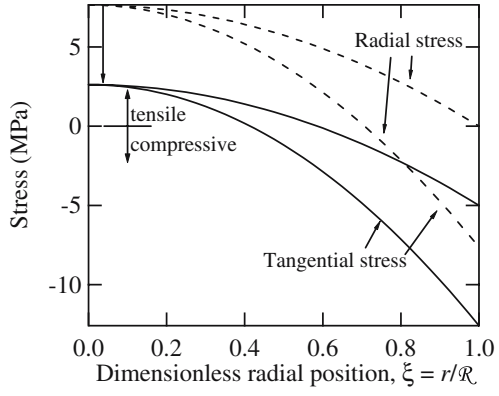

Fig. 10 Simulated stress profiles in the particle at the end of lithium insertion, with no external pressure (*dashed curves*) and with an applied external pressure of 5 MPa. The simulation parameters are the same as those given in Table 1, except that C=10C (I=0.05).

This fit is valid over the experimentally measured domain $0.01 < x_{\mathrm{LiS}} < 0.99$. The OCP is plotted as a function of x_{LiS} in Fig. 12, along with the corresponding thermodynamic factor, which is calculated from the OCP by Eq. (133). It is evident from the figure that plateaus in the OCP, associated with staging in graphite, correspond to thermodynamic factors, and, hence, effective diffusion coefficients, near zero. Peaks in the thermodynamic factor are related to high slopes in the OCP. Although it is difficult to see on the scale shown in the figure, the thermodynamic factor rises dramatically at low values of x_{LiS} to a maximum

[1] The fit is contained in the Fortran program Dualfoil.f, which is available on our website at http://www.cchem.berkeley.edu/~jsngrp. The fit has been modified slightly so as to avoid any regions in which $dU/dx > 0$, which corresponds to a negative thermodynamic factor. Specifically, the coefficient of the fourth hyperbolic tangent has been changed from 0.0351 to 0.0347.

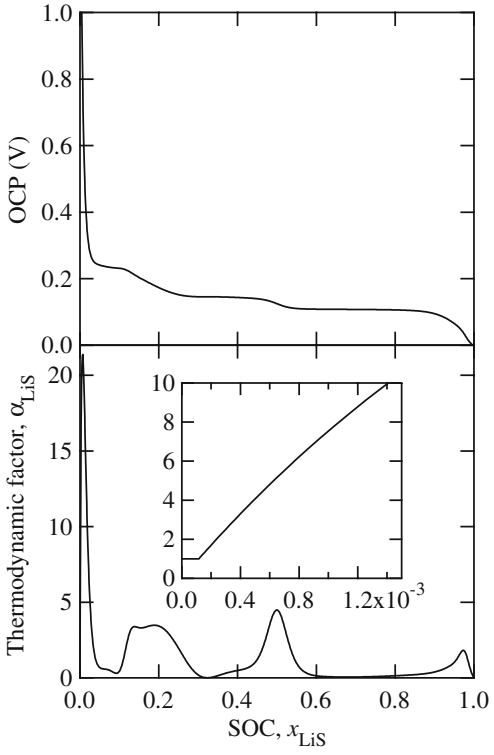

Fig. 12 OCP and the thermodynamic factor, as a function of SOC, for graphite, according to the fit given in Eq. (120).

of 22 at $x_{LiS} = 0.01$. For the simulations described here, the thermodynamic factor was set equal to 1 for $x_{LiS} < 1.16 \times 10^{-4}$, as shown in the inset, to capture the ideal nature of the dilute limit. This was necessary to ensure convergence at low SOCs, at which the pressure diffusion term and the empirically derived thermodynamic factor would otherwise be too small for there to be a significant driving force for diffusion. This underscores a limitation of the empirical fit for the OCP, which cannot be measured accurately in the dilute limit.

While it is possible to calculate the dilute limit of the OCP from Eq. (133), assuming a thermodynamic factor of unity for $x_{LiS} < 1.16 \times 10^{-4}$, this correction should have no impact on the galvanostatic simulations, which are independent of the OCP, and has little impact even on potentiostatic simulations, for which the dilute limit constitutes only a small fraction of the simulated SOC interval. A dilute-limit correction could also be made for high SOCs (i.e., $x_{LiS} > 0.98$), but all of the simulations for Li_xC_6 are limited to $x_{LiS} < 0.6$.

The exchange current density is also dependent upon the OCP, and is therefore a function of the SOC. This potential dependence is typically not included in electrochemical kinetics, but a thermodynamically rigorous derivation of the Butler–Volmer expression shows that for a nonideal solid solution (i.e., one that does not have a Nernstian OCP), the exchange current density does not vary smoothly with lithium concentration in the solid.

Figure 13 shows the dimensionless exchange current density as a function of SOC in three cases: curve a is the exchange current density for an ideal solid solution, curve b is that for a nonideal solution in which the OCP is used but the activity coefficient of vacant host material is assumed to be constant, and curve c is that for a nonideal solution in which activity coefficients are derived from the thermodynamic OCP. For curve a,

$$I_0 \equiv \frac{i_0}{F k_b^{1-\beta} k_f^{\beta} f_{Li^+,n}^{1-\beta} c_{Li^+}^{1-\beta}} = (1 - x_{LiS})^{1-\beta} x_{LiS}^{\beta}. \tag{121}$$

For curve b [see Eq. (144)],

$$I_0 = k_b^{\beta} k_f^{-\beta} f_{Li^+,n}^{\beta} c_{Li^+}^{\beta} (1 - x_{LiS}) \exp\left(\frac{-\beta F U'}{RT}\right). \tag{122}$$

For curve c [see Eqs. (157), (158), and (159)],

$$I_0 = (1 - x_{LiS})^{1-\beta} x_{LiS}^{\beta} \times \exp\left[-\int_0^{x_{LiS}} \overline{g}(x)dx - (\beta - x_{LiS})\overline{g}(x_{LiS})\right]. \tag{123}$$

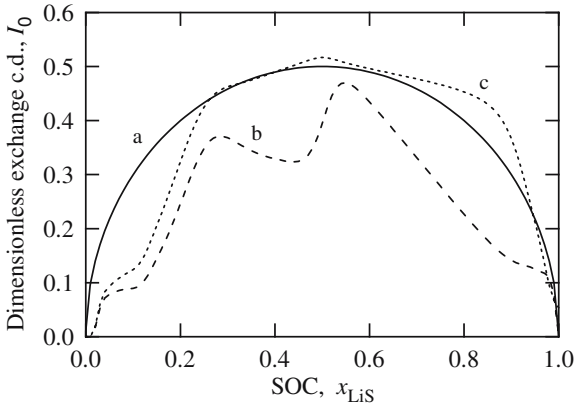

Fig. 13 The dimensionless exchange current density as a function of SOC, according to Eqs. **a** (121), **b** (122), and **c** (123).

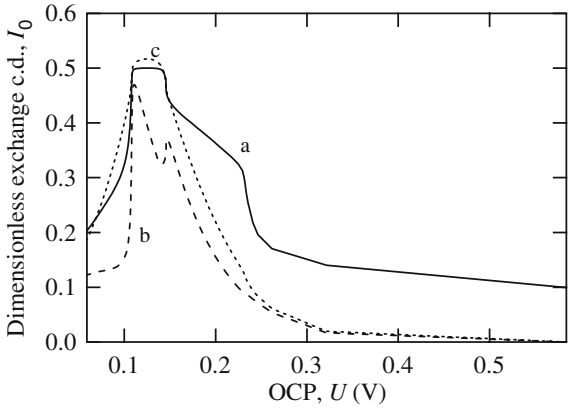

Fig. 14 The dimensionless exchange current density as a function of OCP, according to Eqs. **a** (121), **b** (122), and **c** (123).

Equation (122) is taken from Eq. (144), with γ_S absorbed into k_b. To make a reasonable comparison between the shapes of the three curves, we set the factor $k_b^{\beta}k_f^{-\beta}f_{Li^+,n}^{\beta}c_{Li^+}^{\beta}$ in Eq. (122) equal to 9. We further assume that the concentration of lithium cations is equal to the reference concentration, so that the thermodynamic OCP is identical to the measured OCP.

Figure 14 shows the three exchange current densities as a function of OCP. Here, the deviation of the ideal case (curve a) from the nonideal case (curve c) is more apparent, especially at high potential.

The boundary condition [Eq. (105)], which relates the current density to the flux of lithium, has been altered for the potentiostatic charge and discharge simulations represented in Figs. 15, 16, 17, and 18. The dimensionless potentiostatic boundary condition is derived in the Appendix and is repeated here:

$$\mathcal{N}_{LiS} - \theta x_{LiS}\frac{d\chi}{d\tau} = \delta(1-x_{LiS})^{1-\beta}x_{LiS}^{\beta}\Gamma(x_{LiS}) \times \{\exp[(1-\beta)H] - \exp(-\beta H)\} \text{ at } \xi = 1. \quad (124)$$

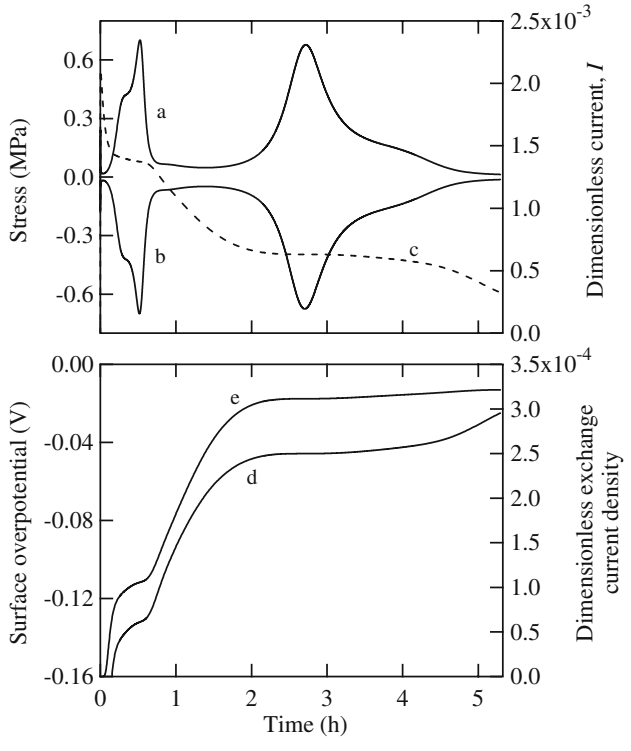

Fig. 15 **a** The maximum radial stress (at ξ=0), **b** minimum tangential stress (at ξ=1), **c** dimensionless current density, **d** surface overpotential, and **e** dimensionless exchange current density during potentiostatic lithium insertion. The potential is set to 0.1 V vs lithium, $\delta k_b^{1/2}k_f^{-1/2}f_{Li^+,n}^{1/2}c_{Li^+}^{1/2} = 0.01$, and Eq. (120) is used for the OCP. All other parameters are given in Table 1. Nonidealities are included in the exchange current density and the thermodynamic factor.

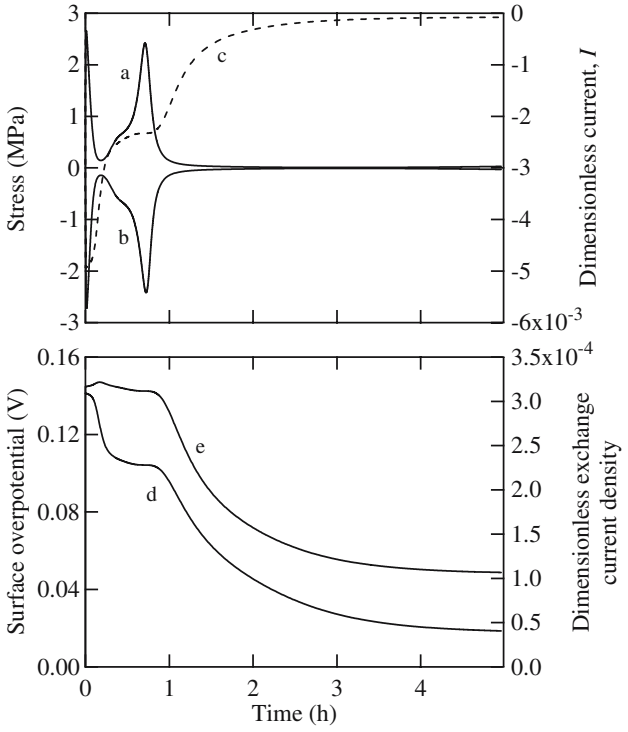

Fig. 16 **a** The maximum tangential stress (at ξ=1), **b** minimum radial stress (at ξ=0), **c** dimensionless current density, **d** surface overpotential, and **e** dimensionless exchange current density during potentiostatic lithium extraction. The potential is set to 0.25 V vs lithium, $\delta k_b^{1/2}k_f^{-1/2}f_{Li^+,n}^{1/2}c_{Li^+}^{1/2} = 0.01$, the initial SOC is 0.6, and Eq. (120) is used for the OCP. All other parameters are given in Table 1. Nonidealities are included in the exchange current density and the thermodynamic factor.

$\Gamma(x_{LiS})$, H, and δ are given by Eqs. (159), (162), and (163), respectively, and β is a symmetry factor, assumed to be equal to1/2. $\Gamma(x_{LiS})$ is a function of SOC that contains the influence of any solid–solid interactions, which are absent from an ideal solid solution. For a Nernstian OCP, $\Gamma = 1$. δ can be thought of as the dimensionless ratio of mass-transport resistance to kinetic resistance. It replaces I in the dimensionless parameter count. The inclusion of β adds one to the number of parameters.

Figures 15 and 16 show the maximum stress responses during potentiostatic lithium insertion and extraction, respectively, with the thermodynamic factor and exchange current density calculated from the OCP given in Eq. (120). For insertion, the potential was set to 0.1 V, with the initial SOC, $x_{LiS0} = 0$, and for extraction it was set to 0.25 V, with $x_{LiS0} = 0.6$. Not all of the lithium would be extracted at this potential, but it yields a comparable average overpotential for the two simulations. The simulations are ended once the average SOC has been changed by 0.5.

The dimensionless current is also plotted in Figs. 15 and 16, while the surface overpotential and dimensionless exchange current density are plotted in the lower portion of the figures. As the dimensionless current decreases in magnitude, the stress in the particle generally decreases, as expected, with peaks in the stress arising due to valleys in the thermodynamic factor (see Fig. 19). Regions of low

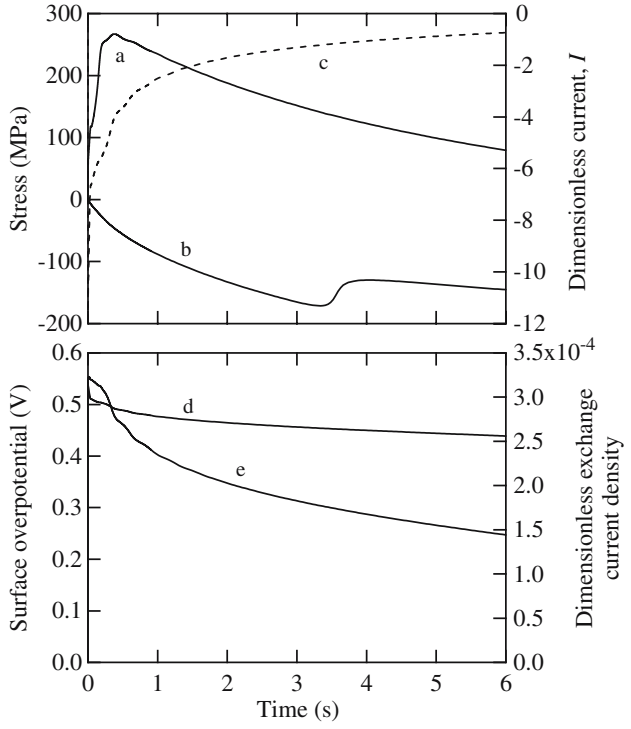

Fig. 17 **a** The maximum tangential stress (at ξ=1), **b** minimum radial stress (at ξ=0), **c** dimensionless current density, **d** surface overpotential, and **e** dimensionless exchange current density during potentiostatic lithium extraction. The potential is set to 0.65 V vs lithium, $\delta k_b^{1/2} k_f^{-1/2} f_{Li^+,n}^{1/2} c_{Li^+}^{1/2} = 0.01$, the initial SOC is 0.6, and Eq. (120) is used for the OCP. All other parameters are given in Table 1. Nonidealities are included in the exchange current density and the thermodynamic factor.

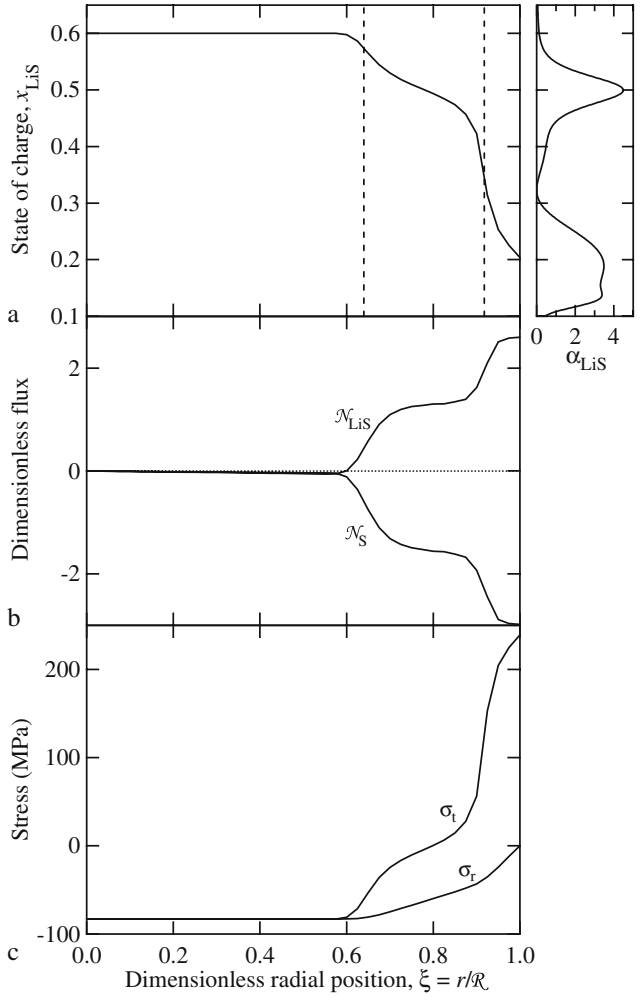

Fig. 18 Profiles of **a** SOC, **b** dimensionless flux, and **c** stress during potentiostatic extraction, at t=0.9 s. Nonidealities are included in the exchange current density and thermodynamic factor. The potential was set to 0.65 V, and the initial SOC is 0.6. Other parameters are given in Table 1.

thermodynamic factor derive from plateaus in the material's OCP as a function of SOC ($dU/dx_{LiS} = 0$), according to Eq. (133). A point at which the slope in the OCP is exactly equal to zero (i.e., the thermodynamic factor is equal to zero) is known as a consolute point, or critical mixing point, and has been examined theoretically [25–29] and experimentally [30, 31] for binary liquid systems. The plateaus in the OCP in turn correspond closely to plateaus in the dimensionless current, which is why the stress components peak at the current density plateaus. These features are clearly visible in the case of both insertion and extraction, which occur over a moderate time scale (5 h), corresponding to the moderate dimensionless current shown in the figures.

The time required for insertion of 0.5 unit of lithium per C_6 unit at 0.1 V is slightly greater than that for extraction of the same amount at 0.25 V, even though the average absolute value of overpotential is higher in the former case (71 mV vs 51 mV).[2] Moreover, the peak stresses are higher for extraction, and the dimensionless current decays more rapidly. Because the driving force for insertion/extraction, and therefore the current, increases with the exponential of the absolute value of the dimensionless overpotential, one might assume that the stress peaks would be higher and that the current would decay faster for the simulation with the higher overpotential, i.e., insertion. This discrepancy is resolved by including the effect of the exchange current density, which, for extraction, happens to be large at SOCs, for which the overpotential is high in magnitude. For insertion, on the other hand, the exchange current density is close to zero when the overpotential is at its highest magnitude, and the overpotential is small when the exchange current density is high. Hence, the average product of the exchange current density and the exponential term containing the overpotential is much greater for extraction. This demonstrates the importance of including nonidealities in the calculation of the exchange current density.

The choice of potential for potentiostatic extraction of lithium deserves some special consideration. One might choose a higher potential to remove more lithium. Figure 17 shows the stress evolution, dimensionless current, OCP,

[2] Although it is not shown on the potential scale of Fig. 15, which has been expanded to compare it with the overpotential for extraction (Fig. 16), the overpotential for insertion (Fig. 15) starts at less than −1.65 V.

and dimensionless exchange current density for a simulation of extraction with an applied voltage of 0.65 V. At this potential, extraction occurs much more rapidly, and the timescale for the current density decay shown in Fig. 17 is only 6 s. The dimensionless current over this period is on the order of 1 to 10, indicating that the diffusion timescale (90 s) is much greater than the extraction timescale. Thus, the features of the stress response are dominated by the diffusion process. At such high dimensionless currents, the concentration profile is not fully developed by the time a considerable fraction of lithium has been extracted, as evidenced by the lack of symmetry between the radial and tangential stresses. The first peak in radial stress at the center of the sphere lags the peak in tangential stress at the surface due to the finite time required for diffusion.

Figure 18 shows the mole-fraction, dimensionless flux, and stress profiles in the particle at $t = 0.9$ s. Here, we see that much of the lithium has been extracted in the region $\xi > 0.6$, whereas the SOC in the region $\xi < 0.6$ is near its initial value of 0.6. Moreover, the shape of the profile is dictated by the variation in the thermodynamic factor with x_{LiS}, which is shown to the right of the mole-fraction profile. Because the diffusivity is low where the thermodynamic factor is low, the corresponding concentration gradient is high. These low-diffusivity regions correspond to plateaus in the OCP (see Fig. 12), which are attributed to staging in the graphite. Hence, we might conclude that steep segments of the mole-fraction profile mark regions in which the graphite transforms from one stage to another. These boundaries are marked by dashed vertical lines, although the transition regions are less distinct than the lines suggest.

Fuller and Newman have calculated concentration profiles near a rotating disk at and around the consolute point of a binary fluid [25, 26]. They show that, at the consolute point, the concentration gradient becomes infinite to yield a finite flux despite the existence of an effective diffusivity of zero. In the solid solution considered here, an OCP fit is used in which consolute points are narrowly avoided (i.e., the slope of the OCP approaches but never equals zero). However, even at a consolute point, the finite pressure-diffusion term, which is independent of the thermodynamic factor, would yield a finite flux without the concentration gradient going to infinity. For both of these reasons, the concentration gradient in Fig. 18a remains finite.

The variation in diffusivity can also be ascertained from the dimensionless flux profiles, with steps corresponding to rapid increases in the thermodynamic factor. The fluxes are both slightly negative in the unreacted region, $\xi < 0.6$, because the material is being compressed there, although there is no significant diffusion occurring in the region. The stress profiles show corresponding behavior, with constant negative stress for $\xi < 0.6$. Physically, one can view this as a compression of the particle core due to the shell shrinking around it.

The negative electrode or the entire cell would not be discharged potentiostatically during practical battery operation; however, positive electrode materials such as lithium manganese oxide undergo volume reduction (lithium extraction) during cell charging. In this case the sort of behavior exhibited in Figs. 16, 17, 18 is relevant, although different thermodynamic properties should be used.

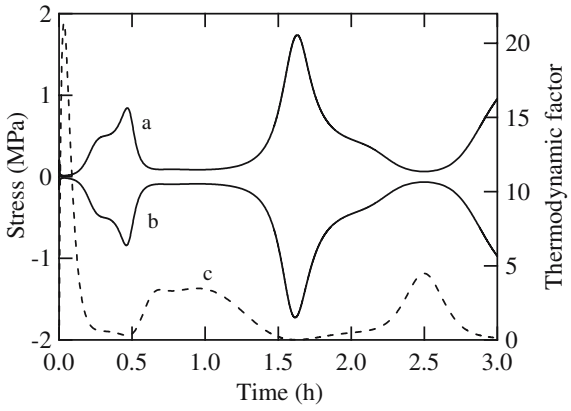

Fig. 19 The **a** maximum radial stress (at ξ=0), **b** minimum tangential stress (at ξ=1), and **c** thermodynamic factor during lithium insertion. Eq. (120) is used for the OCP, and the assumption that α_{LiS}=1 is relaxed. All other parameters are given in Table 1.

Figure 19 highlights the effect that the thermodymanic factor has on the stress evolution for galvanostatic insertion. It is clear that peaks in the stress correspond to low thermodynamic factors, whereas a high thermodynamic factor, which corresponds to a high rate of diffusion and low dimensionless current, results in minimal stress. Because the thermodynamic factor is less than one for some states of charge, the stress peaks are higher than the maximum stress achieved when nonidealities are not taken into account (compare with Fig. 5). Of equal importance is the fact that the variation in thermodynamic factor leads to cycling of the strain and stress over the course of insertion. Such cyclic strains may reduce the tensile and compressive strengths of the material over time. Thus, because the stress oscillates more when nonidealities are included than when they are neglected, it is expected that the inclusion of nonidealities

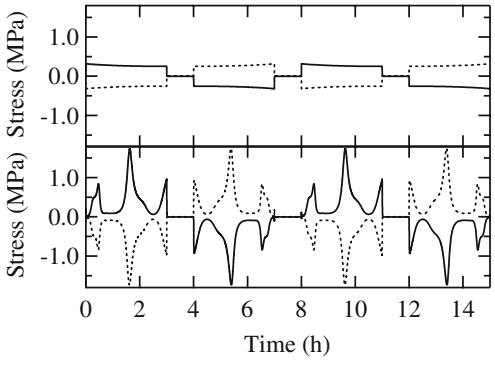

Fig. 20 Maximum stresses generated during two galvanostatic insertion/extraction cycles. The *upper plot* shows the radial stress at ξ=0 (*solid curve*) and tangential stress at ξ=1 (*dashed curve*) for an ideal solution (α_{LiS}=1). The *lower plot* shows the radial stress at ξ=0 (*solid curve*) and tangential stress at ξ=1 (*dashed curve*) for a particle with nonidealities ($\alpha_{\mathrm{LiS}}\neq$1). The cycle profile used for the simulation was: 3-h charge, 1-h rest, 3-h discharge, 1-h rest, 3-h charge, 1-h rest, and 3-h discharge. Eq. (120) was used for the OCP, and other parameters are given in Table 1.

will predict the onset of fracture sooner than if nonidealities were neglected.

Figure 20 elucidates this issue by showing two sequential galvanostatic insertion/extraction cycles for an ideal solution (upper plot), in which the thermodynamic factor is a constant, equal to 1, and for a nonideal solution (lower plot), in which the thermodynamic factor is calculated from the OCP. The cycle profile consists of 3-h charge and discharge segments, separated by 1-h open-circuit relaxation periods. Because the dimensionless current is low, and diffusion effects vanish on a short timescale compared to insertion and extraction, the second cycle is identical to the first. Over the two cycles, each component of stress has only four extrema in the ideal case, while there are 10 local maxima and 10 local minima in the nonideal case. In this tally, we neglect the small spikes at the beginning of charge and end of discharge, which are artifacts resulting from the constant value of the thermodynamic factor at SOCs less than 1.16×10^{-4}. The higher frequency of cycling in the latter scenario should decrease the life of the particle, or at least hasten the occurrence of morphological changes.

The figure also illustrates the importance of carefully selecting the SOC range over which a high-power application is operated. HEV batteries are typically operated over a narrow SOC range close to a depth of discharge of 50%. For a material with variable diffusivity, it is desirable to operate over an SOC range where the diffusivity is highest, not only because this results in fewer transport limitations, but also because it minimizes the stress generated in the material.

Figure 21 shows the maxima in the two stress components, as functions of dimensionless current, from simulations in which a varying thermodynamic factor was included. The maxima for the ideal-solution simulations (see Fig. 7) are included for comparison. The arrow indicates the HEV example (arrow b from Fig. 7), corresponding to a charge rate of 5C and particle radius of 5 μm. By considering nonidealities, one can conclude that fracture is likely under these conditions. Another way of stating this

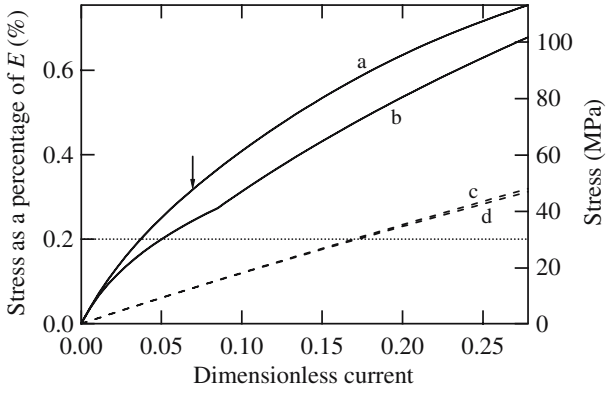

Fig. 21 The maximum **a** tensile and **b** compressive stresses calculated using a thermodynamic factor based upon Eq. (120) and the maximum **c** tensile and **d** compressive stresses calculated using a thermodynamic factor of unity, as a function of dimensionless current. The *arrow* marks the dimensionless current corresponding to a 5-μm particle radius and 5C charge rate.

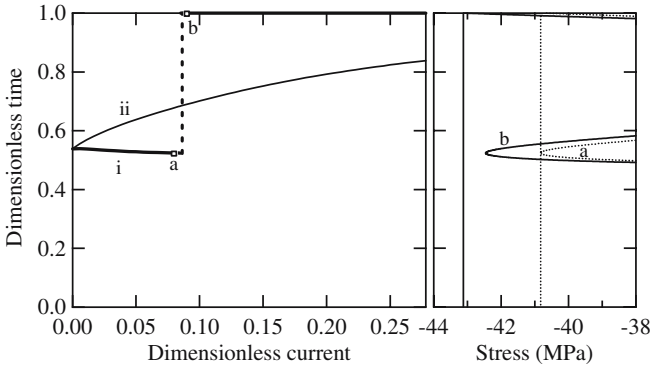

Fig. 22 *The plot on the left* shows the dimensionless time at which the *i* minimum tangential and *ii* maximum radial stress components are reached during lithium insertion, as a function of dimensionless current. *The plot on the right* shows the tangential stress as a function of dimensionless insertion time at two distinct dimensionless currents corresponding to the *open boxes* in the left plot. The dimensionless currents considered were **a** 0.08 and **b** 0.09. The *vertical line* in the right plot serves as a guide to show which peak is the absolute minimum for each of the dimensionless currents.

is that including nonidealities reduces by 78% the maximum allowable dimensionless current. This underscores the importance of considering nonideal behavior of the solid solution.

A subtle but interesting feature of the maximum tangential stresses shown in Fig. 21 is that the curve bows at $I=0.089$, then straightens out. By comparison, the curves for the ideal case vary smoothly. The shape of the nonideal curves is explored in more detail in Fig. 22. The left side of the figure shows the normalized time ($t^*=t/t_{tot}$), as a fraction of the total insertion time (t_{tot}), at which the maxima are obtained for each dimensionless current that was simulated. The time varies smoothly at low dimensionless currents, but there is a discontinuity in the time at

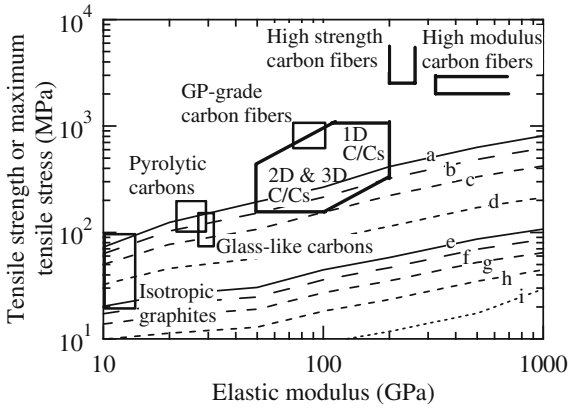

Fig. 23 Typical tensile strengths and elastic moduli of carbonaceous materials, along with simulated tensile-stress maxima. The *curves* show maximum stresses achieved in the simulations for dimensionless currents (5-μm particle radius charge rates) of **a** 0.222 (16C), **b** 0.167 (12C), **c** 0.111 (8C), **d** 5.56×10^{-2} (4C), **e** 2.78×10^{-2} (2C), **f** 2.22×10^{-2} (1.6C), **g** 1.67×10^{-2} (1.2C), **h** 1.11×10^{-2} (C/1.25), and **i** 5.56×10^{-3} (C/2.5). Simulations were performed with various elastic moduli. The material properties represented by the *boxes* are taken from Inagaki [17]. Disordered MCMB is included in the isotropic graphite category.

which the maximum tangential stress is obtained. This discontinuity occurs because, as the shape of the stress response varies with dimensionless current, the stress maxima hop from one peak to the next, as shown on the right side of Fig. 22. This plot shows the tangential stress minima on an expanded scale for two dimensionless currents, 0.08 and 0.09. These currents correspond to the two open boxes in Fig. 22, each of which is in a separate region on the curve for the minimum tangential stress. Here we see that at $I = 0.08$, the minimum stress is at the bottom (earliest) peak, while at $I = 0.09$, the minimum is at the end of charge.

Figure 23, adapted from Inagaki [17], gives the elastic modulus and tensile strength of a broad range of carbonaceous materials. Disordered MCMB falls in the isotropic graphite category. The curves represent simulated maximum tensile stresses that arise during lithium insertion at various dimensionless currents. The curves are slightly crooked due to the peak-hopping phenomenon illustrated in Fig. 22. As the dimensionless current is increased from 5.56×10^{-3} (curve i) to 0.222 (curve a), the maximum stress for a given elastic modulus increases. For a particle with $R_0 = 5$ μm, these dimensionless currents correspond to charge rates ranging from C/2.5 to 16C. At charge rates above 4C (curve e), the tensile strength for some types of carbon is surpassed, meaning fracture is likely for these materials at higher currents. A charge rate of 16C is somewhat greater than the requirements for an HEV application, although such rates may be desirable for future applications. For such high-rate applications, carbon-based negative electrodes can be used only if a smaller particle size is used, or if the material properties could be altered to increase the tensile strength.

Conclusion

A mathematical model for volume expansion and contraction of lithium insertion compounds has been developed, which calculates the stresses that arise during lithium insertion and extraction in lithium-ion-battery operation. High-power applications, such as HEVs, have an increased likelihood of particle fracture compared to low-power applications. Particle fracture can be prevented by reducing the size of the particles, although this tends to accelerate failure in systems that are susceptible to side reactions, such as solvent decomposition.

For materials that expand during lithium insertion, such as carbon and manganese oxide, the particle surface is most likely to fracture at the end of extraction, while the center is most likely to fracture near the beginning of lithium insertion, once the concentration profile is fully developed. Although this is true for ideal solutions, nonideal solutions do not follow this trend exactly, and the time at which the peak stress is obtained depends upon the lithium–host interactions, as well as the applied potential in the case of potentiostatic charging.

Our simulations demonstrate that pressure-diffusion is significant and must be accounted for when calculating the rate of lithium diffusion and magnitude of stress generation. Although it only weakly affects the stress maxima obtained during full insertion and extraction, the role of pressure diffusion becomes relevant for cells that are cycled between intermediate SOC limits. The actual contribution of pressure diffusion depends upon how the partial molar volumes vary with composition.

Furthermore, nonidealities embodied in the thermodynamic factor and, under potentiostatic conditions, the exchange current density have a significant impact on the charge and discharge behavior, including the stress response. The variation of stress due to the variation in the thermodynamic factor is particularly important when considering material fatigue due to strain cycling.

List of symbols

a_i	Activity of species i
a_i^θ	Activity of species i at a secondary reference state
C	C rate, h^{-1}
c	Total concentration, mol/m^3
c_0	Composition-dependent component of concentration, mol/m^3
c_i	Concentration of species i, mol/m^3
D	Dimensionless ratio of diffusive to elastic energy
$\mathcal{D}_{\mathrm{LiS,S}}$	Binary diffusion coefficient, m^2/s
$\underline{d}_{\mathrm{LiS}}$	Thermodynamic driving force, N/m^3
E	Elastic modulus, N/m^2
$\mathbf{E}^*$	Eulerian strain
e	Dilatational strain; dimensionless elastic modulus
F	Faraday's constant, 96,487 C/mol
G	Total Gibbs function, J
g	Nonideal correction to Nernstian OCP, V
$\overline{g}$	Dimensionless correction to Nernstian OCP
I	Dimensionless current
I_0	Dimensionless exchange current density
I_p	Current per particle, A
i	Current density, A/m^2
i_0	Exchange current density, A/m^2
k_f	Forward rate constant, mol/m^2-s
k_b	Backward rate constant, m/s
M_i	Molar mass of species i, g/mol
$\overline{M}$	Molar-mass ratio
N_i	Molar flux of species i, mol/m^2-s
$\mathcal{N}_\mathrm{i}$	Dimensionless molar flux of species i
n_i	Number of moles of species i, mol
p	Pressure, N/m^2
p_0	External hydrostatic pressure, N/m^2
R	Gas constant, 8.314 J/mol-K
$\mathcal{R}$	Particle radius, m
$\mathcal{R}_0$	Initial particle radius, m
r	Radial coordinate, m
r'	Radial position, m
r_0	Initial radial position, m
$\overline{S}_i$	Partial molar entropy of species i, J/mol-K
T	Temperature, K
T_i	Total stress, N/m^2
t	Time, s
U	OCP, V

U^{θ}	Standard cell potential, V
$\overline{U}$	Dimensionless OCP
u	Displacement, m
$\overline{u}$	Dimensionless displacement
V	Cell potential, V
$\overline{V}_i$	Partial molar volume of species i, m^3/mol
$\overline{V}^*_{\mathrm{LiS}}$	Partial molar volume ratio
$\underline{v}_i$	Velocity of species i, m/s
w	Radial gradient of u
x_i	Mole fraction of species i
$x_{\max}$	Maximum SOC
y	Stretched coordinate
z	Time derivative of u, m/s
α	Thermodynamic factor
β	Symmetry factor
γ	Mole-fraction activity coefficient
δ	Dimensionless reference exchange current density
δ_{ij}	Kronecker delta
ε	Strain
ζ	Dimensionless time derivative of u
H	Dimensionless surface overpotential
η_{s}	Surface overpotential, V
θ	Dimensionless total concentration
κ	Compressibility, m^2/N
λ	Lamé constant, N/m^2
μ	Lamé constant, N/m^2
μ_i	Chemical potential of species i, J/mol
μ_i^{θ}	Secondary reference chemical potential of species i, J/mol
ν	Poisson's ratio
ξ	Dimensionless radial position
π	Dimensionless pressure
ρ	Density, g/m^3
ρ_{s}^0	Density of pure B, g/m^3
σ	Normal elastic stress, N/m^2
$\overline{\sigma}$	Dimensionless stress
τ	Dimensionless time
χ	Dimensionless particle radius
ω	Fractional expansivity

Subscripts

LiS	Lithium intercalated host material
r	Radial
S	Unoccupied host material
t	Tangential

Acknowledgements This work was supported by the Assistant Secretary for Energy Efficiency and Renewable Energy, Office of FreedomCAR and Vehicle Technologies of the US Department of Energy under Contract No. DE-AC02-05CH11231.

Appendix

Thermodynamics and kinetics

For lithium insertion into a generic host material, we consider the following reversible electrochemical reaction:

$$\mathrm{LiS} \rightarrow \mathrm{Li}^+ + \mathrm{e}^- + \mathrm{S}, \tag{125}$$

where S represents the host material. The OCP, U, of the intercalation material relative to a lithium reference is given by the equation

$$FU = \mu^0_{\mathrm{Li}} + \mu_{\mathrm{S}} - \mu_{\mathrm{LiS}}, \tag{126}$$

where F is Faraday's constant and μ^0_{Li} is the chemical potential of pure lithium metal, which does not depend upon the composition of the host material. As in Eq. (6), the chemical potential of a species can be expressed in terms of its mole fraction, activity coefficient, and secondary reference chemical potential:

$$\mu_i = \mu_i^{\theta} + RT \ln (\gamma_i x_i). \tag{127}$$

Expanding the chemical potentials in Eq. (126), we have

$$FU = FU^{\theta} + RT \ln \left(\frac{x_{\mathrm{S}}}{x_{\mathrm{LiS}}} \right) + RT \ln \left(\frac{\gamma_{\mathrm{S}}}{\gamma_{\mathrm{LiS}}} \right), \tag{128}$$

where

$$FU^{\theta} = \mu^0_{\mathrm{Li}} + \mu^{\theta}_{\mathrm{S}} - \mu^{\theta}_{\mathrm{LiS}}. \tag{129}$$

Differentiating Eq. (126) with respect to x_{LiS} yields

$$F \frac{\partial U}{\partial x_{\mathrm{LiS}}} = \frac{\partial \mu_{\mathrm{S}}}{\partial x_{\mathrm{LiS}}} - \frac{\partial \mu_{\mathrm{LiS}}}{\partial x_{\mathrm{LiS}}}. \tag{130}$$

The species S and LiS are not independent of each other; the amounts of the two species sum to a constant, and their chemical potentials are related by the Gibbs–Duhem equation:

$$x_{\mathrm{LiS}} d\mu_{\mathrm{LiS}} + x_{\mathrm{S}} d\mu_{\mathrm{S}} = 0. \tag{131}$$

Thus, Eq. (130) becomes

$$\frac{\partial \mu_{\mathrm{LiS}}}{\partial x_{\mathrm{LiS}}} = -F(1 - x_{\mathrm{LiS}}) \frac{\partial U}{\partial x_{\mathrm{LiS}}}. \tag{132}$$

Applying Eq. (7), the thermodynamic factor is therefore

$$1+\frac{\partial \ln \gamma_{\mathrm{LiS}}}{\partial \ln x_{\mathrm{LiS}}}=\frac{x_{\mathrm{LiS}}}{RT}\frac{\partial \mu_{\mathrm{LiS}}}{\partial x_{\mathrm{LiS}}} =-\frac{F}{RT}x_{\mathrm{LiS}}(1-x_{\mathrm{LiS}})\frac{\partial U}{\partial x_{\mathrm{LiS}}}. \tag{133}$$

For an ideal solution,

$$U=U^{\theta}+\frac{RT}{F}\ln\left(\frac{1-x_{\mathrm{LiS}}}{x_{\mathrm{LiS}}}\right), \tag{134}$$

and the thermodynamic factor is unity. The derivation shown here follows the development of Darling [32], and avoids invoking the excess free energy, which is used by Verbrugge and Koch to derive a similar relationship between the thermodynamic factor and OCP via interaction parameters [33]. Our approach is more general than that of Verbrugge and Koch, in that it accommodates the wide variety of empirical OCP fits available in the literature. However, care must be taken when the empirical fits do not correctly approach the dilute limits or when they result in negative values for the thermodynamic factor.

A kinetic model is required to determine the effect of nonidealities in the electrode and electrolyte upon the exchange current density. Typically, the concentrations of reactants and products are used, but here, we use their activities for the sake of generality. The current associated with reaction Eq. (125) (i.e., lithium insertion into a generic host material) can be expressed as

$$i=F\left[k_{\mathrm{f}}' a_{\mathrm{LiS}}\exp\left(\frac{(1-\beta)FV}{RT}\right)-k_{\mathrm{b}}' a_{\mathrm{S}} a_{\mathrm{Li^+}}\exp\left(\frac{-\beta FV}{RT}\right)\right], \tag{135}$$

where a_{LiS} and a_{S} are activities of lithium-filled and lithium-void sites in the host material, respectively; $a_{\mathrm{Li^+}}$ is the activity of lithium ions in solution; k_{f}' and k_{b}' are the forward and backward rate constants, respectively; and V is the difference between the electrode potential and the potential in the solution near the electrode, relative to a lithium reference electrode in contact with electrolyte of a particular lithium ion concentration (e.g., 1 M).

The thermodynamic OCP is obtained by setting the current to zero:

$$k_{\mathrm{f}}' a_{\mathrm{LiS}}\exp\left(\frac{(1-\beta)FU'}{RT}\right)=k_{\mathrm{b}}' a_{\mathrm{S}} a_{\mathrm{Li^+}}\exp\left(\frac{-\beta FU'}{RT}\right). \tag{136}$$

We emphasize that U' is different from the measured OCP given in Eq. (128), which is independent of the activity of lithium ions. In describing solid diffusion phenomena in the electrode, the activity of lithium ions is irrelevant and can be set arbitrarily to the reference activity.

We can rearrange Eq. (136) to solve for the forward rate preexponential factor:

$$k_{\mathrm{f}}' a_{\mathrm{LiS}}=k_{\mathrm{b}}' a_{\mathrm{S}} a_{\mathrm{Li^+}}\exp\left(\frac{-FU'}{RT}\right). \tag{137}$$

Substituting this expression into Eq. (135), we have

$$i=Fk_{\mathrm{b}}' a_{\mathrm{S}} a_{\mathrm{Li^+}}\exp\left(\frac{-\beta FU'}{RT}\right) \times\left[\exp\left(\frac{(1-\beta)F\eta_{\mathrm{s}}}{RT}\right)-\exp\left(\frac{-\beta F\eta_{\mathrm{s}}}{RT}\right)\right], \tag{138}$$

where

$$\eta_{\mathrm{s}}=V-U' \tag{139}$$

is the surface overpotential of the reaction. Equations (137) and (138) can subsequently be combined to yield

$$i=F\left(k_{\mathrm{f}}' a_{\mathrm{LiS}}\right)^{\beta}\left(k_{\mathrm{b}}' a_{\mathrm{S}} a_{\mathrm{Li^+}}\right)^{1-\beta} \times\left[\exp\left(\frac{(1-\beta)F\eta_{\mathrm{s}}}{RT}\right)-\exp\left(\frac{-\beta F\eta_{\mathrm{s}}}{RT}\right)\right]. \tag{140}$$

The activities of the solid species are given by

$$a_i=a_i^{\theta}\gamma_i x_i, \tag{141}$$

where a_i^{θ} is the activity at a particular secondary reference state (i.e., it is a function of temperature and pressure, but not of composition), and γ_i is the mole fraction activity coefficient. For lithium ions, we use an activity that is independent of electrical state. That is,

$$a_{\mathrm{Li^+}}=a_{\mathrm{Li^+},n}^{\theta} f_{\mathrm{Li^+},n} c_{\mathrm{Li^+}}, \tag{142}$$

where $a_{\mathrm{Li^+},n}^{\theta}$ and $f_{\mathrm{Li^+},n}$ are, respectively, the reference activity and activity coefficient of lithium ions with respect to a reference species, n, in solution (see Eq. 3.19 of reference [34]). The reference species must be ionic, and, in our binary electrolyte, is limited to lithium ions and the corresponding anion. Because the reference electrode used here is lithium metal, lithium ions are the natural choice for the reference ion. Accordingly,

$$f_{\mathrm{Li^+},n}=\frac{f_{\mathrm{Li^+}}}{f_{\mathrm{Li^+}}^{\mathrm{ref}}}, \tag{143}$$

where $f^{\text{ref}}_{\text{Li}^+}$ is the ionic activity coefficient at the reference concentration of lithium ions (i.e., the concentration adjacent to the reference electrode). The ratio does not depend upon an ill-defined electrical state, and therefore, neither does the activity of lithium ions used in the kinetic model. Note that with this choice of reference ion, $a^{\theta}_{\text{Li}^+,n} = 1$.

From the above definitions of activity, Eqs. (138) and (140) can be expressed as

$$i = Fk_{\text{b}}\gamma_{\text{S}}x_{\text{S}}f_{\text{Li}^+,n}c_{\text{Li}^+}\exp\left(\frac{-\beta FU'}{RT}\right) \times\left[\exp\left(\frac{(1-\beta)F\eta_{\text{s}}}{RT}\right)-\exp\left(\frac{-\beta F\eta_{\text{s}}}{RT}\right)\right] \tag{144}$$

and

$$i = Fk_{\text{f}}^{\beta}k_{\text{b}}^{1-\beta}\gamma_{\text{LiS}}^{\beta}\gamma_{\text{S}}^{1-\beta}x_{\text{LiS}}^{\beta}x_{\text{S}}^{1-\beta}\left(f_{\text{Li}^+,n}c_{\text{Li}^+}\right)^{1-\beta} \times\left[\exp\left(\frac{(1-\beta)F\eta_{\text{s}}}{RT}\right)-\exp\left(\frac{-\beta F\eta_{\text{s}}}{RT}\right)\right], \tag{145}$$

where $k_{\text{f}} = k'_{\text{f}}a^{\theta}_{\text{LiS}}$ and $k_{\text{b}} = k'_{\text{b}}a^{\theta}_{\text{S}}$. Equation (145) is the familiar Butler–Volmer equation, with the preexponential group constituting the exchange current density.

Solving for U' in Eq. (137), using the Eqs. (141) and (142) for the activities, we have

$$U' = U'^{\theta} + \frac{RT}{F}\ln\left(\frac{x_{\text{S}}}{x_{\text{LiS}}}\right) + \frac{RT}{F}\ln\left(\frac{\gamma_{\text{S}}}{\gamma_{\text{LiS}}}\right) + \frac{RT}{F}\ln\left(f_{\text{Li}^+,n}c_{\text{Li}^+}\right), \tag{146}$$

where

$$U'^{\theta} = \frac{RT}{F}\ln\left(\frac{k_{\text{b}}}{k_{\text{f}}}\right). \tag{147}$$

In contrast to the reference potential given in Eq. (128), this term is complicated by the fact that the ratio $k_{\text{b}}/k_{\text{f}}$ has units of inverse molarity. Essentially, it is the reference potential from Eq. (128), with the dependence upon lithium ion concentration removed. This is why we distinguish between the thermodynamic U' and the measured U; the latter has no ionic composition dependence. Section 5.7 of reference [34] elaborates further upon this subject.

Presumably, the OCP is Nernstian in the limit of small LiC_6 concentration. That is,

$$\lim_{x_{\text{LiS}}\to 0}U' = U'^{\theta} + \frac{RT}{F}\ln\left(\frac{x_{\text{S}}}{x_{\text{LiS}}}\right) + \frac{RT}{F}\ln\left(f_{\text{Li}^+,n}c_{\text{Li}^+}\right). \tag{148}$$

Let $g(x_{\text{LiS}})$ represent the deviation from Nernstian behavior over the entire stoichiometric range of the material. In other words, let

$$U' = U'^{\theta} + \frac{RT}{F}\ln\left(\frac{x_{\text{S}}}{x_{\text{LiS}}}\right) + \frac{RT}{F}\ln\left(f_{\text{Li}^+,n}c_{\text{Li}^+}\right) + g(x_{\text{LiS}}). \tag{149}$$

Comparing Eq. (149) with Eq. (146), we see that

$$g(x_{\text{LiS}}) = \frac{RT}{F}\ln\frac{\gamma_{\text{S}}}{\gamma_{\text{LiS}}}. \tag{150}$$

From the Gibbs–Duhem equation [Eq. (131)] and the relationship between the chemical potential of a species and its thermodynamic factor [Eq. (7)], we can show that the thermodynamic factor for species S is identical to the thermodynamic factor for species LiS. Hence, by Eq. (133), we have

$$1 + \frac{\partial\ln\gamma_{\text{S}}}{\partial\ln x_{\text{S}}} = -\frac{F}{RT}x_{\text{LiS}}(1-x_{\text{LiS}})\frac{\partial U'}{\partial x_{\text{LiS}}}. \tag{151}$$

Here, we have made use of the fact that the dependence of U' upon x_{LiS} is identical to that of U.

In defining our reference state, we specify that the activity coefficient of a species approaches unity in the limit of dilute lithium (i.e., vacant host material):

$$\gamma_i \to 1 \text{ as } x_{\text{LiS}} \to 0. \tag{152}$$

Thus, rearranging and integrating (151) yields:

$$\gamma_{\text{S}} = \frac{1}{1-x_{\text{LiS}}}\exp\left(-\frac{F\left[\int_0^{x_{\text{LiS}}}U'(x)dx - x_{\text{LiS}}U'(x_{\text{LiS}})\right]}{RT}\right). \tag{153}$$

Insertion of this result into Eq. (144) yields

$$i = Fk_{\text{b}}f_{\text{Li}^+,n}c_{\text{Li}^+} \times\exp\left(-\frac{F\left[\int_0^{x_{\text{LiS}}}U'(x)dx + (\beta - x_{\text{LiS}})U'(x_{\text{LiS}})\right]}{RT}\right) \times\left[\exp\left(\frac{(1-\beta)F\eta_{\text{s}}}{RT}\right)-\exp\left(\frac{-\beta F\eta_{\text{s}}}{RT}\right)\right]. \tag{154}$$

The resulting exchange current density is a function of electrode composition via the OCP:

$$i_0 = Fk_{\text{b}}f_{\text{Li}^+,n}c_{\text{Li}^+} \times\exp\left(-\frac{F\left[\int_0^{x_{\text{LiS}}}U'(x)dx + (\beta - x_{\text{LiS}})U'(x_{\text{LiS}})\right]}{RT}\right). \tag{155}$$

Substituting Eq. (149) into (155), we can write the exchange current density in terms of the nonideal portion of the OCP:

$$i_0 = Fk_{\mathrm{b}}^{1-\beta}k_{\mathrm{f}}^{\beta}f_{\mathrm{Li}^+,n}^{1-\beta}c_{\mathrm{Li}^+}^{1-\beta}(1-x_{\mathrm{LiS}})^{1-\beta}x_{\mathrm{LiS}}^{\beta} \times \exp\left(-\frac{F\left[\int_0^{x_{\mathrm{LiS}}} g(x)dx + (\beta - x_{\mathrm{LiS}})g(x_{\mathrm{LiS}})\right]}{RT}\right). \tag{156}$$

In dimensionless form,

$$I_0 = (1-x_{\mathrm{LiS}})^{1-\beta}x_{\mathrm{LiS}}^{\beta}\Gamma(x_{\mathrm{LiS}}). \tag{157}$$

where

$$I_0 = \frac{i_0}{Fk_{\mathrm{b}}^{1-\beta}k_{\mathrm{f}}^{\beta}f_{\mathrm{Li}^+,n}^{1-\beta}c_{\mathrm{Li}^+}^{1-\beta}}, \tag{158}$$

$$\Gamma(x_{\mathrm{LiS}}) = \exp\left[-\int_0^{x_{\mathrm{LiS}}}\overline{g}(x)dx - (\beta - x_{\mathrm{LiS}})\overline{g}(x_{\mathrm{LiS}})\right], \tag{159}$$

and

$$\overline{g} = \frac{Fg}{RT}. \tag{160}$$

For potentiostatic lithium extraction and insertion, the galvanostatic boundary condition Eq. (105) is replaced with

$$\mathcal{N}_{\mathrm{LiS}} - \theta x_{\mathrm{LiS}}\frac{d\chi}{\tau} = \delta(1-x_{\mathrm{LiS}})^{1-\beta}x_{\mathrm{LiS}}^{\beta}\Gamma(x_{\mathrm{LiS}}) \times \{\exp[(1-\beta)\mathrm{H}] - \exp(-\beta\mathrm{H})\} \quad \text{at } \xi = 1, \tag{161}$$

where

$$\mathrm{H} = \frac{F\eta_{\mathrm{s}}}{RT} \tag{162}$$

and

$$\delta = \frac{k_{\mathrm{b}}^{1-\beta}f_{\mathrm{Li}^+,n}^{1-\beta}c_{\mathrm{Li}^+}^{1-\beta}k_{\mathrm{f}}^{\beta}\mathcal{R}_0 M_{\mathrm{s}}}{\mathcal{D}_{\mathrm{LiS,S}}\rho_{\mathrm{S}}^0}. \tag{163}$$

References

1. Beaulieu LY, Eberman KW, Turner RL, Krause LJ, Dahn JR (2001) Electrochem Solid State Lett 4:A137
2. Thomas KE (2002) Dissertation. University of California, Berkeley
3. Ohzuku T, Tomura H, Sawai K (1997) J Electrochem Soc 144:3496
4. Sawai K, Yoshikawa K, Tomura H, Ohzuku T (1998) Prog Batteries Battery Mater 17:201
5. Kostecki R, McLarnon F (2003) J Power Sources 119:550
6. Hirschfelder JO, Curtiss CF, Bird RB (1954) Molecular theory of gases and liquids. Wiley, New York, p 714 (corrected printing with notes added, 1964)
7. Curtiss CF, Bird RB (1999) Ind Eng Chem Res 38:2515
8. Battaglia VS (1993) Dissertation. University of California, Berkeley
9. Kröger FA, Vink HJ (1956) In: Seitz F, Turnbull D (eds) Solid state physics: advances in research and applications, vol 3. Academic, New York, p 310
10. Kröger FA, Vink HJ (1958) J Phys Chem Solids 5:208
11. Malvern LE (1969) Introduction to the mechanics of a continuous medium. Prentice-Hall, Englewood Cliffs, p 159
12. Bird RB, Stewart WE, Lightfoot EN (2002) Transport phenomena. Wiley, New York, p 19
13. Timoshenko S (1934) Theory of elasticity. McGraw-Hill, New York, p 203
14. Garcia RE, Chiang YM, Carter WC, Limthongkul P, Bishop CM (2005) J Electrochem Soc 152:A255
15. Boresi AP (1965) Elasticity in engineering materials. Prentice-Hall, Englewood Cliffs, p 71
16. Ogumi Z, Inaba M (2002) In: van Schalkwijk WA, Scrosati B (eds) Advances in lithium-ion batteries, vol. Kluwer/Plenum, New York, p 79
17. Inagaki M (2000) New carbons: control of structure and functions. Elsevier, New York, p 199
18. Billaud D, McRae E, Hérold A (1979) Mater Res Bull 14:857
19. Kganyago KR, Ngoepe PE (2003) Phys Rev B 68:205111
20. Nicklow R, Smith HG, Wakabaya N (1972) Phys Rev B 5:4951
21. Hertzberg RW (1996) Deformation and fracture mechanics of engineering materials. Wiley, New York, p 526
22. Winter M, Besenhard JO, Albering JH, Yang J, Wachtler M (1998) Prog Batteries Battery Mater 17:208
23. Zaghib K, Nadeau G, Kinoshita K (2000) J Electrochem Soc 147:2110
24. Winter M, Novák P, Monnier A (1998) J Electrochem Soc 145:428
25. Fuller TF, Newman J (1993) Int J Heat Mass Transfer 36:347
26. Fuller TF (1992) Dissertation. University of California, Berkeley
27. Levich VG (1962) Physicochemical hydrodynamics. Prentice-Hall, Englewood Cliffs, NJ
28. Sengers JV (1972) Ber Bunsen Ges 76:234
29. Cussler EL (1976) Multicomponent diffusion. Elsevier, New York
30. Krichevsky IR, Tshekhanskaya YV (1956) Zhurnal Fizicheskoi Khimii 30:2315
31. Vitagliano V, Sartorio R, Chiaravalle E, Ortona O (1980) J Chem Eng Data 25:121
32. Darling RM (1998) Dissertation. University of California, Berkeley
33. Verbrugge MW, Koch BJ (1996) J Electrochem Soc 143:600
34. Newman J, Thomas-Alyea KE (2004) Electrochemical systems. Wiley-Interscience, Hoboken